HELSINGIN YLIOPISTO
HELSINGFORS UNIVERSITET
UNIVERSITY OF HELSINKI

Spatial distribution and evolution of porosity in a heterogeneous clay-rich fault core

M.Sc. thesis

VILLE NENONEN

NOVEMBER 2018

DEPARTMENT OF GEOSCIENCES AND GEOGRAPHY

HELSINGIN YLIOPISTO – HELSINGFORS UNIVERSITET – UNIVERSITY OF HELSINKI

Tiedekunta/Osasto – Fakultet/Sektion – Faculty	Laitos – Institution – Department
Faculty of Science	Department of Geosciences and Geography

Tekijä – Författare – Author
Ville Nenonen

Työn nimi – Arbetets title – Title
Spatial distribution and evolution of porosity in a heterogeneous clay-rich fault core

Oppiaine – Läroämne – Subject
Geology

Työn laji – Arbetets art – Level	Aika – Datum – Month and Year	Sivumäärä – Sidoantal – Number of Pages
M.Sc. Thesis	November 2018	61

Tiivistelmä – Referat – Abstract

Sedimentary clay rocks present impermeable, low-porosity formations, often having a seal function to hydrocarbon reservoirs and geological repositories. Due to their impermeable properties, these shale beds can act as a barrier to fluid flow. However, shale formations are intruded by fault zones with permeabilities that can differ of several orders of magnitudes with respect to the undeformed host rock. The fault core comprises of several structures, including breccias, cataclasites and one or several slip surfaces. The slip surface of a fault consists of clay gouge that is heterogeneous material with anisotropic properties in terms of porosity and permeability. The fault core with clay-gouge can act as a barrier or as a lengthwise conduit to fluid flow, depending on physical and chemical properties of a fault. For these reasons, the distribution of porosity in fault core is a key parameter for many applications, including hydrocarbon reservoir capacity, geothermal energy projects and geological repositories for CO_2 or high-level radioactive waste.

The objective of this work is to combine information on spatial distribution of porosity provided by the ^{14}C-PMMA autoradiography method with the mineralogical information provided by a comprehensive SEM-EDS elemental mapping and to define the porosity variations in and around fault gouges and connect them to processes in a fault system. The samples used in this study were taken from a small-scale vertical strike-slip fault in an argillaceous shale formation at the Tournemire underground research laboratory, Southern France. The results display significant variations in porosity and mineralogy along the studied gouge zone, most probably due to a polyphased tectonic history and paleo-fluid migrations. The studied gouge expresses low porosities in the central part, but porosity values increase significantly in the margins of the gouge. Moreover, the mineralogical changes indicate sealing/healing effects and past hydrothermal activities within the fault zone. The sealing effect is displayed by distribution of calcium as calcite, which is concurrent with lower porosities around the gouge zone. The EDS analysis reveals the zonality of iron and existence of zinc sulphide and barium sulphate inside the gouge, further suggesting hydrothermal activity in the past. Furthermore, the zonality of iron is coherent with different porosity areas as it has formed concentration bands around the areas of low-porosity gouge. Even though the observed porosity variations occur in only a centimetre-wide gouge zone, the higher porosity sections may imply pathways for fluid flow if the fault is reactivated.

Avainsanat – Nyckelord – Keywords
Porosity, clay mineralogy, gouge, fault structure, permeability, XRD, SEM-EDS, C-14-PMMA

Säilytyspaikka – Förvaringställe – Where deposited
University of Helsinki library

Muita tietoja – Övriga uppgifter – Additional information

HELSINGIN YLIOPISTO – HELSINGFORS UNIVERSITET – UNIVERSITY OF HELSINKI

Tiedekunta/Osasto – Fakultet/Sektion – Faculty	Laitos – Institution – Department	
Matemaattis-luonnontieteellinen	Geotieteiden ja maantieteen osasto	
Tekijä – Författare – Author		
Ville Nenonen		
Työn nimi – Arbetets title – Title		
Huokoisuuden jakautumisen kehitys heterogeenisessa savirikkaassa siirrosytimessä		
Oppiaine – Läroämne – Subject		
Geologia		
Työn laji – Arbetets art – Level	Aika – Datum – Month and Year	Sivumäärä – Sidoantal – Number of Pages
Pro Gradu	Marraskuu 2018	61

Tiivistelmä – Referat – Abstract

Savikivet ovat heikosti läpäiseviä ja vähähuokoisia muodostumia ja toimivat usein sulkevana kerroksena hiilivetyesiintymille ja geologisille loppusijoitustiloille. Savikivet voivat läpäisemättömien ominaisuuksiensa vuoksi toimia esteenä fluidien kierrolle maankuoressa. Savikivimuodostumissa esiintyvillä siirroksilla voi kutienkin olla huomattavasti deformoitumatonta isäntäkiveä korkeampia läpäisevyysarvoja. Siirrosydin voi koostua useista eri rakenteista, esimerkiksi breksioista, kataklasiiteista ja yhdestä tai useammasta siirrospinnasta. Siirrospinnoilla esiintyy usein savi-gougea, jolla on anisotrooppiset huokoisuus- ja läpäisevyysominaisuudet. Savipitoinen siirrosydin voi estää tai johtaa fluideja, riippuen siirroksen fysikaalisista ja kemiallisista ominaisuuksista. Näistä syistä huokoisuusjakauma savirikkaissa siirrosytimissä on tärkeä muuttuja monissa kohteissa; esimerkiksi hiilivetyesiintymiä kartoittaessa, geotermisissä energiaprojekteissa ja hiilidioksidin tai korkea-aktiivisen ydinjätteen loppusijoitustilaa suunniteltaessa.

Tämän työn tarkoituksena on yhdistää ^{14}C-PMMA autoradiografialla saadut huokoisuusarvot SEM-EDS alkuainekartoitukseen ja määrittää huokoisuuden ja mineralogian vaihtelut siirros-gougeissa sekä niiden ympärillä. Nämä huokoisuusvaihtelut pyritään yhdistämään siirroksiin vaikuttaviin prosesseihin. Työssä käytetyt näytteet on otettu pienestä sivuttaissiirroksesta argilliitti-savikivestä Tournemiren maanalaisesta tutkimuslaboratoriosta Etelä-Ranskassa. Tulokset näyttävät merkittäviä huokoisuuden ja mineralogian vaihteluita tutkitun gouge-alueen poikki. Nämä vaihtelut johtuvat todennäköisesti monimutkaisesta tektonisesta historiasta ja useista fluidimigraatioista. Gougen keskellä huokoisuus on matalaa, mutta huokoisuuden arvot nousevat huomattavasti reunoilla. Lisäksi mineralogia viittaa siirroksen mineraalisulkeutumiseen ja hydrotermiseen fluidikiertoon. Siirroksen sulkeutuminen näkyy kalsiumin jakautumisena kalsiittina matalimman huokoisuuden alueilla. EDS-analyysi antaa viitteitä raudan vyöhykkeisyydestä sekä sinkkisulfidien ja bariumsulfaattien esiintymisestä siirrosytimessä. Näiden mineraalien esiintyminen osoittaa, että siirroksessa on todennäköisesti esiintynyt hydrotermistä fluidikiertoa menneisyydessä. Lisäksi raudan vyöhykkeet ovat matalimman huokoisuuden gougen ympärillä, mikä viittaa todennäköisesti hydrotermiseen kiertoon. Vaikka havaitut huokoisuusvaihtelut esiintyvät vain senttimetrin levyisellä gougealueella, korkeamman huokoisuuden vyöhykkeet voivat toimia fluidikierron mahdollistavina reitteinä, jos siirros aktivoituu uudelleen.

Avainsanat – Nyckelord – Keywords

Huokoisuus, savimineralogia, gouge, siirroksen rakenne, läpäisevyys, XRD, SEM-EDS, C-14-PMMA

Säilytyspaikka – Förvaringställe – Where deposited

Helsingin yliopiston kirjasto

Muita tietoja – Övriga uppgifter – Additional information

CONTENTS

1. INTRODUCTION

Shales and argillites are pelitic sedimentary rocks with dominantly clay-rich mineralogy, micro- or nanoscale mineral grain sizes and preferred orientation of mineral grains along the bedding, depending on the amount of overburden stress. Due to the small grain sizes and mineral orientations of clays, clay-rocks have intrinsically low permeability. However, these formations are commonly crosscut by fault zones. These fault zones produce a high anisotropy in terms of crustal fluid flow in otherwise isotropic and impermeable conditions in sedimentary clay rocks and thus control the migration of these fluids (Faulkner et al., 2010; Wibberley et al., 2008; Caine et al., 1996). In the brittle stress regime close to the surface, these zones are lithologically heterogeneous, anisotropic in terms of permeability and discontinuous. The permeability in a fault zone is a product of spatial and temporal processes which strongly depend on the host-rock lithology, stress and strain rate, deformation mechanisms, the fault architecture and many more parameters. For instance, shale deformation under high effective stress may lead to its compaction and decreased porosity and permeability, whereas when over-consolidated clay deforms under low effective stress, the same rock may dilate and have an increase in permeability due to increased pore volume (Holland et al., 2006).

The fault zone is divided into segments of high (fault core) and low strain rates (damage zone) (Faulkner et al., 2010). A high strain core usually consists of severely deformed rocks (formed of brecciated lenses from fault wall) and typically one or more principal slip surfaces. In low-grade metamorphic rocks, such surfaces consist of fault gouges. The gouge is a fine-grained heterogeneous material with a high anisotropy in terms of porosity and permeability (Engelder, 1974). The primary mechanism for the generation of gouge is cataclasis and other deformation processes occurring during fault shearing in brittle or brittle-ductile stress regime in low temperature close to the surface (Vrolijk and Van Der Pluijm, 1999; Engelder, 1974). Cataclastic deformation is a brittle-frictional mechanism involving grain granulation by frictional grain boundary sliding and grain fracturing (Knipe, 1989; Engelder, 1974). The remaining grains are surrounded by fine grained matrix of crushed material (Chester et al. 1993; Engelder, 1974).

Clay gouges typically support lower shear stresses and have low frictional resistance with constrained pore fluid movement and elevated pore pressures (Morrow et al., 1984). For these reasons, an active fault with clay gouges may favor creep behavior instead of rupturing and earthquake propagation. Especially fault slip surfaces with smectite and other swelling clays have been suggested to significantly weaken the fault, as smectite can act as a lubricant to promote weak behavior and in faults (Van Der Pluijm, 2011). However, faults tend to heal and seal over time with cementation filling the fissures left open by fault movement. Healing process can increase the strength of a fault as the cementations generally have higher friction coefficients (e.g. Wibberley et al., 2008). Furthermore, fault healing processes can seal the fault and leading to overpressure of pore fluids. Compaction of gouge under hydrostatic load and/or during shearing can elevate pore pressures in sealed fault and allow seismic sliding at low shear stresses (Byerlee, 1993; Blanpied et al., 1992). Structural and mineralogical textures indicate that seismic slips followed by cementation and healing of the fractures and breccia are episodic, leading to cycles of permeability enhancement and reduction and velocity weakening and strengthening along faults (Hickman et al., 1995). The most common clay minerals in pelitic sedimentary rocks are illite and smectite. Fault related shearing may result in smectite to illite- chemical alteration as it can offer energy to overcome the kinetic reaction barrier required for the reaction (Vrolijk and Van Der Pluijm, 1999). Shear induced illitization may lead to increased frictional strength in the fault zone (Saffer and Marone, 2003).

The fault core with clay gouge can act as a barrier or a lengthwise conduit to fluid circulation, depending on the physical and chemical properties of the fault (Faulkner et al., 2010; Wibberley et al., 2008). The fluid flow is an important parameter when making long-term safety assessments for deep geological repositories for high-level radioactive waste and for this reason the porosity distribution of fault zones in clay rocks is under interest. The porosity distribution can be connected straight to fault permeability and fluid migrations. Another application of shale fault porosity include oil and gas industry and storage of CO_2 as the fault permeability is an important parameter for e.g. when making assessments of caprock integrity (e.g. Dockrill and Shipton, 2010).

The repository for nuclear waste requires stable, reducing conditions (Ewing, 2015). The shale formations have naturally very low permeability, stable redox conditions and good sorption capabilities to favor immobilization of radionuclides (Delage et al., 2010). These

properties make shale layers considered potential option in several countries for placement of deep geological repository. Some of potential hosts for repositories are in Callovo-Oxfordian clay formation (France), in Boom Clay (Belgium) and in Opalinus clay (Switzerland) (Laurich et al., 2018; Robinet et al., 2015; Guglielmi et al., 2015a; Laurich et al., 2014; Robinet et al., 2012; Horseman et al., 1987).

The setting of this study was in Tournemire Underground Research Laboratory (URL) in Southwestern France. The Tournemire URL is a laboratory where physical, mechanical and chemical processes affecting the conditions of deep geological repositories are studied extensively (Lefèvre et al., 2016; Constantin et al., 2007; Constantin et al., 2004). The aim in this study was to define the spatial distribution of porosity in heterogeneous, small-scale strike-slip fault core gouge in Tournemire URL. The porosity changes were then linked to mineralogical differences in distinctive domains in the fault core. The spatial porosity distribution and fault core mineralogy were then put into larger bibliographical context to link them to physical and chemical processes in fault systems. The key question was, how small-scale faults can affect the safety of nuclear waste repositories in argillaceous, low permeability formations. C-14-polymethylmethacrylate (C-14-PMMA) autoradiography was applied on samples from the Tournemire fault zone to receive a high-resolution porosity map. Autoradiography is an imaging method based on measuring incoming radiation of a tracer element within the sample. These samples were then analyzed by elemental mapping with a scanning electron microscope (SEM) in a backscatter electron mode (BSE). Additionally, thin sections for optical microscopy and oriented glass-slide samples for X-ray diffraction from clay fractions were prepared. X-ray diffraction (XRD) was used to define the proportions of clay minerals in gouges and adjacent zones.

2. GEOLOGICAL BACKGROUND

2.1. Site description of the Tournemire Underground Research Laboratory

The Toarcian shale formation in the Tournemire Underground Research Laboratory (URL) has been studied extensively by the French Institute of Radiological Protection and Nuclear

Safety (IRSN) in order to examine processes that may play an important role in ensuring the long-term safety of a geological repository.

The Tournemire URL is located in a Mesozoic marine basin on the southern border of the French Massif Central at the western limit of Causse du Larzac (Figure **1.**). The URL is primarily constructed in the Toarcian argillite, an indurated clay formation consisting of shales and marls, with a very low permeability to saturated water flow. The formation shares many characteristics of other indurated clays being considered for radioactive waste disposal, such as the Callovo-Oxfordian argillite in France and the Opalinus Clay in Switzerland (Guglielmi et al., 2015a).

Causse du Larzac is a Permian-Mesozoic N-S basin surrounded by several igneous massifs. The Central massif and Causses area are characterized by volcanism that started during the Paleocene and last until the Holocene (Michon and Merle, 2001). This area has a polyphase tectonic history with at least two major stress regimes (Constantin et al., 2004). The first event was an extension during the Upper Jurassic and the Lower Cretaceous (Constantin et al., 2004). The second event was the Pyrenean compression from Mid-Cretaceous to Eocene (Constantin et al., 2004; Sibuet et al., 2004).

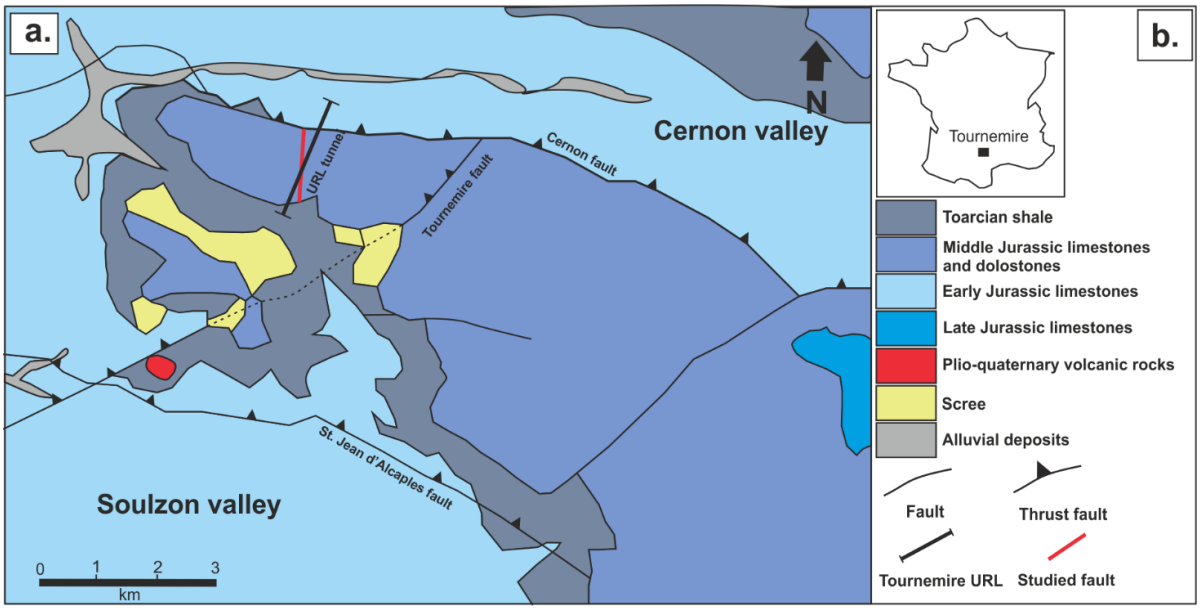

Figure 1. a.: The geological map of Tournemire area in Causse du Larzac. **b.**: The location of Tournemire in France (After Lefèvre et al., 2016).

The Toarcian shale formation found at Tournemire is 250 m thick and located between two active limestone aquifers (Aalenian and Carixian). The shale formation presents low intrinsic

permeability (~10^{-21} – 10^{-18} m^2), significant porosity (~ 9 %) and a strong tendency to show hydraulic 'self-sealing' characteristics post excavation (Matray et al., 2007).

The clay-gouge samples in this study were taken from one drill core that crosses a brittle fault zone in the upper part of Toarcian shale formation of the Tournemire URL (Figure **2.**). The URL is crossed by two main fault zones (F1 and F2) which are separated by undeformed shale (protolith) (Figure **2.**). F1 and F2 have parallel strikes and exhibit similar dip and dip-direction, varying between 170°N to 10°N and 60°W to 80°W respectively (Lefèvre et al. 2016). Slickenfibres from both F1 and F2 indicate that the last movement along these faults has a reversal left-lateral strike-slip component (Peyaud et al., 2006) which is coherent with the last Pyrenean compressive event (Constantin et al., 2004).

The F1 fault zone exhibits an array of anastomosing faults with brittle shear surfaces and ductile shear bands. In contrary, F2 consists of fault core with high strain and displacement (around 3 – 5 m of vertical offset). The F2 fault core is surrounded by an asymmetric damage zone. The internal architecture of F2 is comprised of a protolith; an asymmetric damaged zone (2 – 3 m thick on the western side of the fault) and a core zone (located between the damage zones, ~1 m wide). The fault core of F2 includes fault gouges, cataclasites, breccia, folds and deformed lenses of protolith. The studied gouge (at least three continuous distinct gouge surfaces have been observed, the gouges have different colors from black to grey) forms a thin (1 – 10 mm thick) very fine-grained and non-cohesive zone between the host rock and brecciated lenses of host rock. The slip surfaces of the fault core comprise of gouges and accommodate the highest shear strain and strain localization within the core. The shear zone around the gouge is composed of cataclasites (cohesive rock with angular clasts in a fine-grained matrix) and breccia (fractured and re-cemented country rock). The protolith's mineral composition is relatively homogeneous within the upper Toarcian section, with more than 50 % clay minerals, dominantly illite and illite/smectite, 10 – 20 % calcite, and 10 – 20 % quartz (Dick et al., 2016; Lefèvre et al., 2016; Constantin et al., 2004). Other components (less than 10 %) include detrital micas, feldspars, pyrite and organic carbon (Lefèvre et al., 2016). In contrast, the fault gouge contains predominantly more illite than the surrounding rock (Dick et al., 2016).

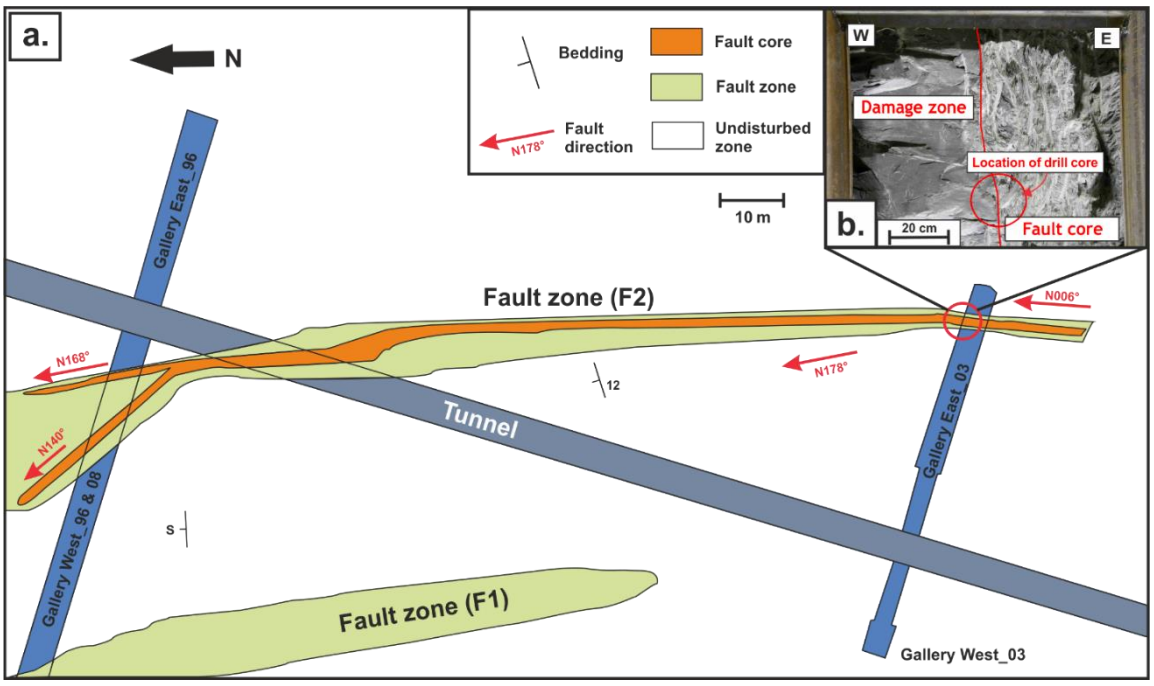

Figure. 2. a.: Structural map of the Tournemire URL. **b.**: Contact between the damage zone and the core zone. The fault core exhibits a high strain area with subvertical schistosity (after Dick et al., 2016).

2.2. Tectonic setting and indicators for past fluid circulations

The Mesozoic extensional event resulted in the activation of the Cernon and St Jean d'Alcapies faults as normal faults and the following Pyrenean compressive event reactivated them as reverse faults (Lefèvre et al., 2016) . During the Pyrenean compressive stress regime, the orientation of σ_1 varied from NE/SW to NW/SE with two adjacent pulses striking 020°N – 030°N and N°160 – N°170 (Constantin et al., 2004). The vertical offset of these faults is 100 – 400 m (Constantin et al., 2004). The features associated with strike-slip faulting in the fault zone of F2 exhibit a dominantly sinistral component (Lefèvre et al., 2016).

The burial depth of the Toarcian shales during the Pyrenean compression are estimated to be a maximum burial depth of 2.3 – 2.4 km (57 – 62 MPa burial stress) at the onset of the Causses basin inversion (Lefèvre et al., 2016; Barbarand et al., 2001). Therefore, the previous studies have concluded that the stress-regime in the studied fault zone during the last strike-slip system was with $\sigma_1 > 70$ MPa, $\sigma_2 \sim 60$ MPa and $\sigma_3 \sim 30 – 40$ MPa (Lefèvre et al., 2016).

The fracture filling minerals in the Tournemire fault zones are predominantly calcite (Lefèvre et al., 2016; Constantin et al., 2007; Constantin et al., 2004). The carbon and oxygen isotope

studies from calcite emphasize two sources for fluids (Peyaud et al., 2006). The first source is the pore fluids of the undeformed Toarcian shale with the same composition than the shale cement, originating from the deposition of detrital particles during sedimentation. The second source is intrusions of meteoric water with influence to the composition of main fault zone veins (Lefèvre et al., 2016). Moreover, Peyaud et al., (2006) observed Fe zonation in fault calcite cement and suggested fluctuating redox conditions within the fault zone during Pyrenean compression. The iron content of calcite may surpass 1%, which indicates that reducing conditions prevailed even after the first infiltrations of meteoric water (Peyaud et al., 2006). This could mean that redox-fluctuations with oxidizing fluids were short-termed and reducing conditions prevailed shortly after an oxidizing fluid intrusion. Zoned carbonate fillings further indicate shifting redox conditions and episodic connections between the fault zone and the overlying Aalenian aquifer (Figure **3.**) (Peyaud et al., 2006).

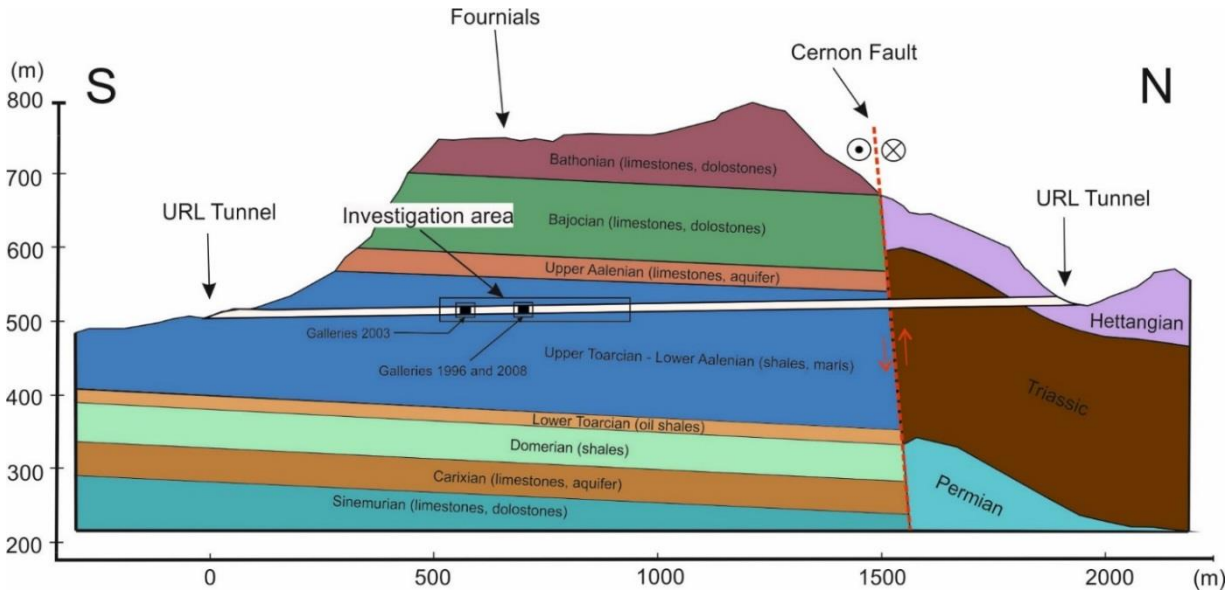

Figure 3. Geological cross-section along the Tournemire URL. The URL tunnel crosscuts the Upper section of the Toarcian shale formation (Modified from Lavielle et al., 2012).

3. MATERIALS AND METHODS

3.1. Sampling at Tournemire URL

In this study, one drill core was used to achieve all the samples. The drill core was extracted parallel to the principal fault plane from the interface between the host shale rock and the fault core zone. A 20 cm diameter borehole was drilled through the boundary between the fault core and the western damage zone parallel to the main fault plane (Figure **4.**). The drill used to extract the core was Hilti and drill fluid was air. The core from this borehole was cut perpendicularly to the fault zone (FZ) into three smaller blocks (length: 42 cm, 20 cm and 8 cm).

In this study the westernmost gouge (Gouge 1) band within the fault core will be presented. This gouge is located at the boundary between the damage zone of the host rock and fault core and may have been formed during the first shearing event connected to the Pyrenean tectonic compression (Lefèvre et al., 2016). Furthermore, another gouge (Gouge 2) band east from the first gouge is presented (Figure **5**.).

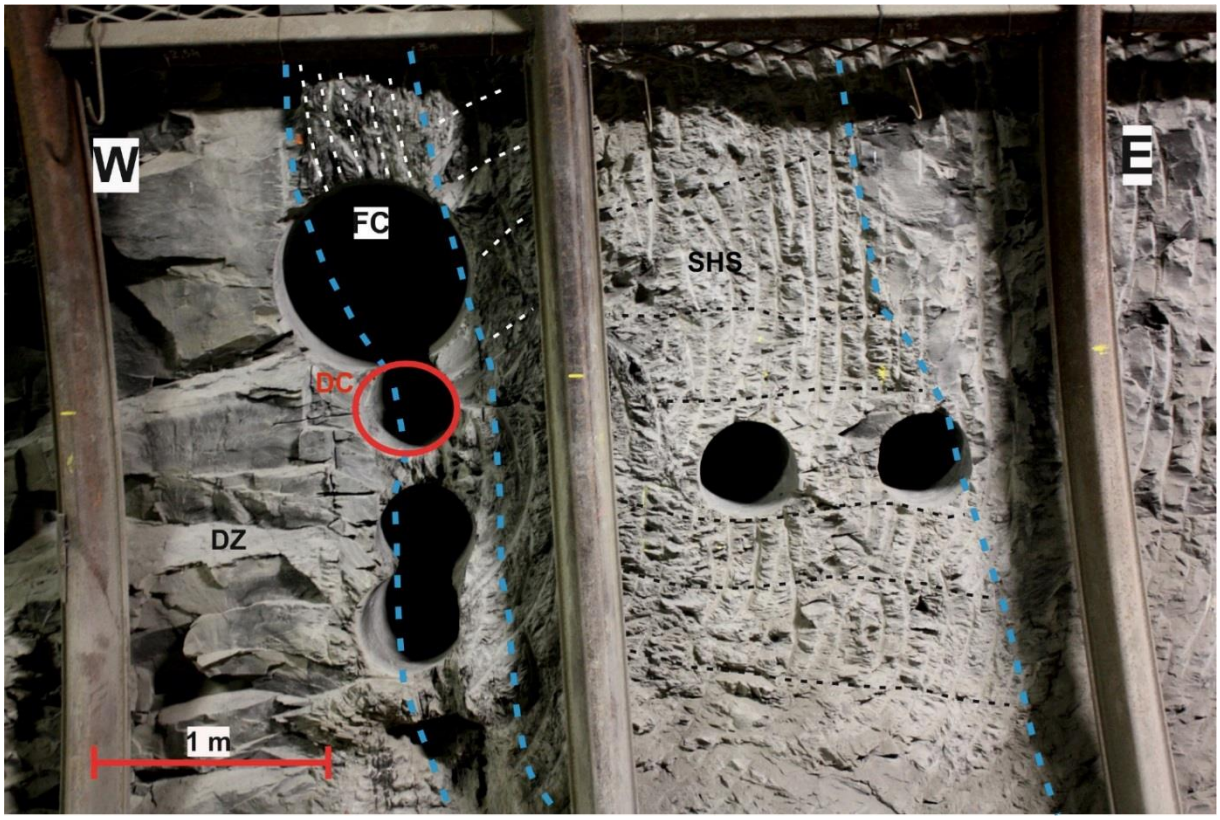

Figure 4. A photograph of the F2 strike-slip fault cross-section in Tournemire shale. Blue crosslines display the margins of the fault core and sub-horizontal schistosity. Abbreviations: DC: The location of the Drill Core used in this study, SHS: Sub-horizontal schistosity, DZ: Damage zone, FC: Fault core. Fault core is here the section with highest strain and vertical foliation. DC bottom with two gouge bands is presented in Figure **5.**

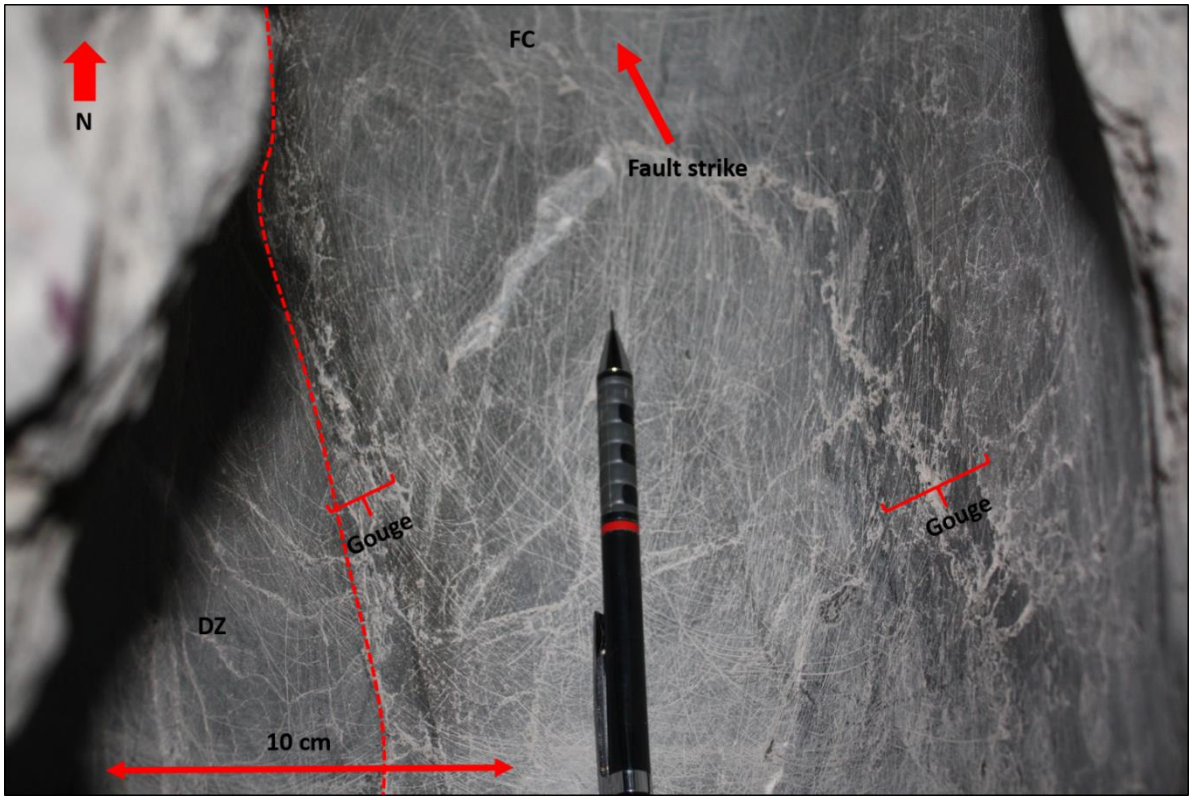

Figure 5. Photograph taken from the inside of Tournemire F2 core hole. Red dash indicates the boundary between the fault core and the damage zone.

3.2. Sample preparation

The 20 cm block obtained from the drill core was cut perpendicularly to the FZ. Next, the core block was encased in epoxy resin to prevent it from fracturing. The horizontally cut block presented three continuous gouge bands and thus was chosen for ^{14}C-PMMA and SEM-EDS analyzes.

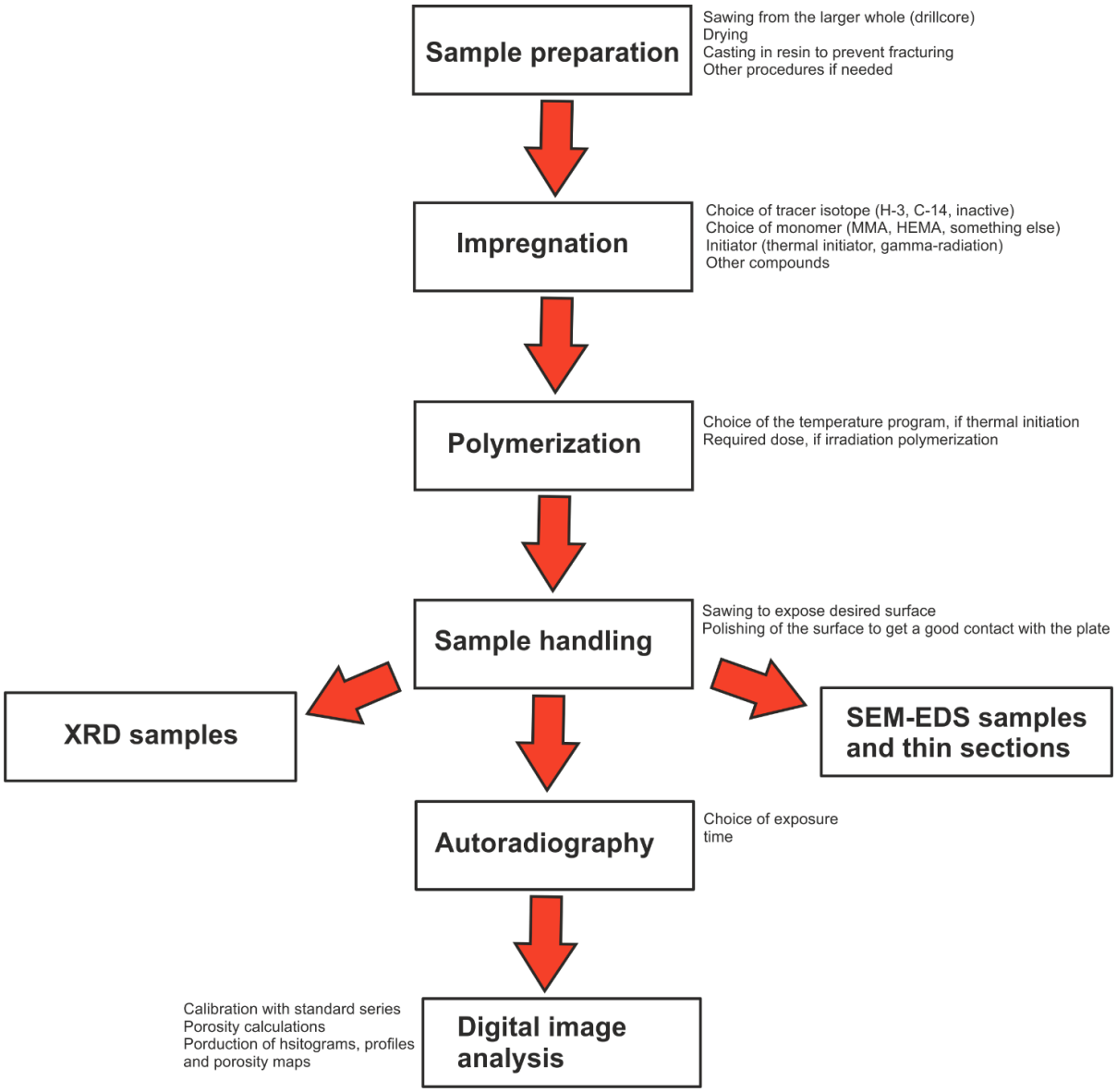

Figure 6. Procedural flow-chart of techniques and work-steps required in this work. The porosity calculations and the spatial distribution of porosity was achieved with ^{14}C-PMMA method, the relative quantities of clay minerals were obtained with X-ray diffraction (XRD) and the mineralogy of different structural domains was observed with Scanning Electron Microscopy (SEM) with Energy Dispersive X-ray Spectroscopy (EDS).

3.2.1 C-14-PMMA autoradiography samples

The samples in this study were impregnated in vacuum in an aluminum cylinder for one month with ^{14}C-labelled MMA resin with an activity of 82 kBq/mL in the Radiochemistry Unit, University of Helsinki. The MMA tracer has a very low viscosity and thus an ability to intrude even the nanoscale porosity. The samples were then irradiated using γ-radiation to polymerize the MMA into PMMA with ^{60}Co source in Estonia (Scandinavian Clinics Estonia OÜ). Samples for the different analyses were then prepared from these polymerized samples. The procedural flow is illustrated in Figure **6**.

Autoradiography was performed on surfaces from samples S1, S2 and S3, as shown in Figure **7**. The SEM-EDS sample surfaces were also autoradiographed. The sample surfaces for autoradiography were produced by sawing the polymerized samples into different subsamples as shown in Figure **7**. These samples were then polished with silicon carbide powder to obtain good contact with the imaging plates. From these samples the different sub-samples were made for XRD, SEM-EDS, X-ray tomography and optical microscopy, as described in their respective sub-chapters.

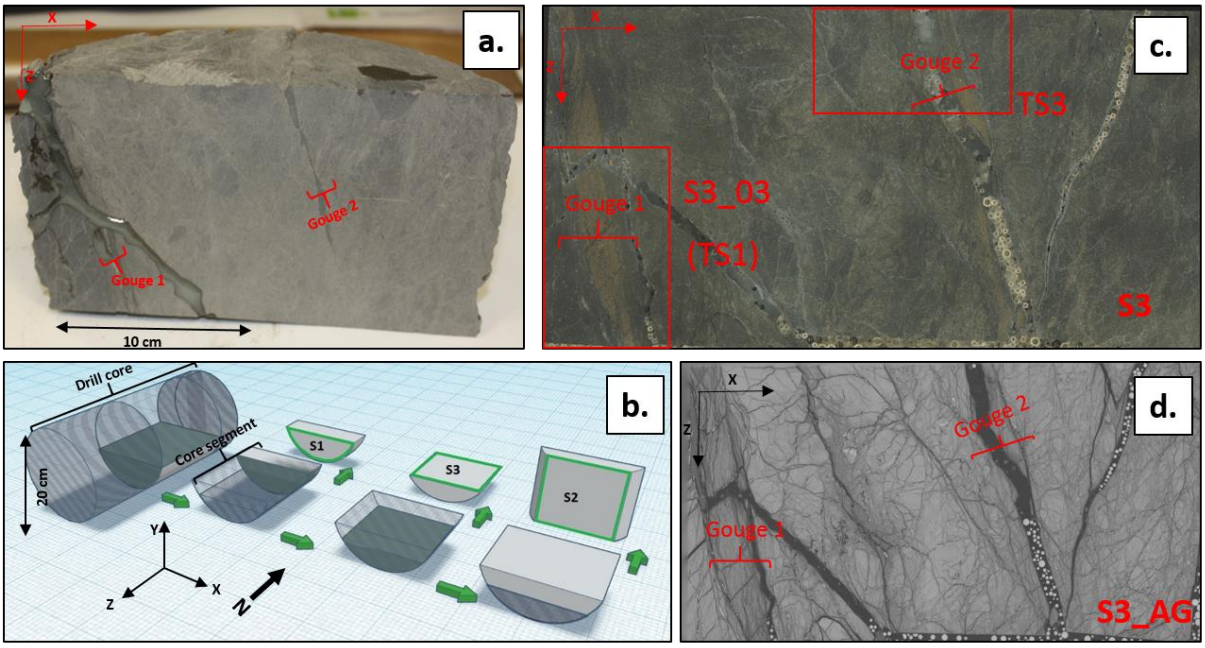

Figure 7. A schematic of sample surfaces for the autoradiography and SEM. **a**.: a photograph of the core segment prior to MMA impregnation. **b**.: a cartoon of sample sawing into sections from the impregnated core segment. The surfaces imaged with autoradiography are bordered with green. The X-Y-Z coordinates are from now on presented on the sample surfaces to present their orientation in respect to the diagram **b**. **c**.: a polished surface of S3 section scanned with a tabletop scanner with placements of samples for SEM-EDS. Sample S3_03 is a thick section investigated with SEM-EDS. TS1 thin section was taken from below the S3_03 thick section. TS3 is a thin section investigated both with SEM-EDS and photomicroscope. **d**.: a porosity map of S3 surface obtained from digital autoradiography (AG). Darker grey values indicate more activity and thus higher porosity. Fissures completely filled with MMA are a sample preparation artefact.

3.2.2. X-ray diffraction samples

For X-ray diffraction, nine samples were prepared on glass slides based on instructions by Poppe et al. (2001). Sample material from sites chosen for XRD characterization were chosen to display the clay mineralogy of two gouges and the adjacent damage zone and breccias between gouges from sample block S2. The material was extracted from the PMMA-impregnated S2 sample surface and milled with a ball mill. The clay fraction (grain size < 2µm)

was separated suspending sample materials into 50ml of distilled water, dispensing larger particles with an ultrasonic probe and finally water-sample suspension was centrifuged. The initial distance R_1 for the centrifuge was 42mm and the final distance R_2 127mm. The water temperature was 22 ºC and acceleration/deceleration time 14 s/10 s with 1000 rounds per minute. The total time for each centrifuging round was 82 seconds. Between each round, suspension was removed with a pipette to another tube and coarser fraction sediment was separated. The suspension was then centrifuged again and repeated for 3-5 times, depending on the transparency of the suspension water. The clay-water suspension was then poured through a filter clog resulting the clay particles forming a layer onto the filter membrane surface. The oriented clay-glass slides were prepared by attaching the filter membrane around a cylinder and rolling the glass slide across the membrane to transfer the clay from the membrane to the slide. Nine powdered samples were made from the Gouge S2 sample block. The samples were extracted from different parts, one from the damaged zone, two from the first gouge, one from the second gouge and the rest from fault breccia between gouges (close to gouge and further away between gouges). The samples were also glycolated with ethylene glycol to reveal the swelling clays and heated to 550 °C for further clay mineral identification. Heat treatment reveals change or loss of structure in clays and can be used to distinguish different clay minerals.

3.2.3. Thin sections

Four thin sections (30 µm thick) for optical microscopy were prepared additionally. Thin section areas were first sawed from the S3 block with a low-speed diamond saw. Then they were glued to a glass slide and excess material was grinded off with a grinder and polished. Additionally, one of the thin sections (TS3) presenting the Gouge zone 2 was chosen for SEM-EDS mapping and coated with carbon. In this work, two thin sections (TS1 and TS3) are presented, as they both contain gouges.

3.3. Optical microscopy

A polarizing microscope with two polarizers was used to inspect different structural domains from the thin sections. The polarizer converts unpolarized light from the microscope lamp. After polarization, light vibrates only in a single direction. Commonly light has a E-W direction parallel to the cross-hair of the ocular when plane-polarized (Pichler and Schmitt-Riegraf,

1997). Polarized light travels through the thin section and occurring changes can be observed with an analyzer (cross-polarizer, with N-S orientation) (Pichler and Schmitt-Riegraf, 1997). First the thin sections were scanned with a tabletop scanner. Then they were investigated in with an optical microscopy (Leica DM 2500P HCX with PL fluotar objectives) with magnifications from 2.5x to 50x, with both plane and cross-polarized light. The areas with changing porosities observed from autoradiograph maps were photographed with Leica application suite and these photographs were contrasted to autoradiograms.

3.4. C-14-PMMA autoradiography technique

C-14-PMMA autoradiography is an imaging method based on intruding an organic monomer liquid, methyl methacrylate (MMA), with radioactive tracer label (^{14}C or ^{3}H) into a sample (L'Annunziata, 2012). The distribution of this radioactive tracer is then characterized using autoradiography techniques, either by film (Hellmuth et al., 1994; Hellmuth et al., 1993) or by digital imaging plate (L'Annunziata, 2012). The method is proven useful to quantify the porosity of media with low porosity or small pore sizes (Siitari-Kauppi, 2002). Contrary to more conventional porosity measurement techniques (e.g. mercury porosimetry), autoradiography can be used to measure spatial distribution of porosity (Sammaljärvi et al., 2016). Even nanometre scale porosity can be measured with C-14-PMMA autoradiography, making it suitable for porosity analysis of sedimentary rock samples (Sammaljärvi et al., 2016; Sardini et al., 2009; Sammartino et al., 2002) and even gouge samples (Prêt et al., 2004).

The measured intensities from the samples are converted into optical densities using Beer-Lambert's law (equation **1.**) (Sammaljärvi et al., 2012),

$$OD_i = -\log\left(\frac{I}{I_0}\right) \qquad \text{(Eq. 1.)}$$

where OD_i is the local optical density, I is the intensity and I_0 is the background intensity. Therefore, in the conversion of intensity into density, the background intensity is taken into account. The optical densities can be converted into activities with the aid of a calibration series with known activity. Such calibration series is presented in Figure **8.** The optical density of the AG-film and the activity can be expressed with equation **2.** (Sammaljärvi, 2017),

$$\boldsymbol{A_i = -\frac{1}{k} * \ln\left(1 - \frac{OD_i - OD_0}{OD_{max}}\right)} \qquad \textbf{(Eq. 2.)}$$

where $\boldsymbol{A_i}$ is a local activity in becquerels, k is a fitting coefficient [Bq^{-1}], $\boldsymbol{OD_i}$ is the local optical density, $\boldsymbol{OD_0}$ the minimum of optical density and $\boldsymbol{OD_{max}}$ is the optical density with a saturated film. Standards are used to calculate $\boldsymbol{OD_0}$, **k** and , $\boldsymbol{OD_{max}}$ for each exposure (Sammaljärvi, 2017). By using equations **1.** and **2.**, the local activity can be solved and placed into equation **3.** The porosity calculations are achieved with equation **3.** However, the beta corrections must be taken into account when calculating porosities. Materials with different densities have a different range of ^{14}C beta-emissions. Therefore, the beta correction is comparable to the grain density of the sample material and to the density of PMMA (Sammartino et al., 2003; Hellmuth et al., 1993). In this work, a grain density for samples was 2.7 g/cm^3 and 1.18 g/cm^3 for PMMA density were used.

$$\boldsymbol{\phi_i} = \frac{\frac{\boldsymbol{\rho_m}}{\boldsymbol{\rho_{resin}}}}{\boldsymbol{1+\frac{A_i}{A_0}*\left(\frac{\rho_m}{\rho_{resin}}-1\right)}} * \boldsymbol{\frac{A_i}{A_0}} \qquad \text{(Eq. 3.)}$$

In equation **3.**, ϕ_i is the local porosity in percentages, ρ_m is the sample grain density (g/cm^3), ρ_{resin} is the PMMA resin density (g/cm^3), A_i is the local activity of the sample (Bq) and A_0 is the activity of the used tracer (Bq). The results of equation **3.** are values between 0 and 1 for each pixel. A pixel with value of zero corresponds to zero porosity and with one, to open space full of pure PMMA. The porosity calculations are completed for all the pixels in the sample surface area and results are exhibited as histograms or porosity profiles (Sammaljärvi, 2017).

The calibration parameters and quantitative porosity calculations were achieved with a program based on Matlab Image analysis toolbox (Sammaljärvi, 2017; Sammaljärvi et al., 2016). A typical AG calibration curve is presented in Figure **9.** Additional contrast to porosity maps can be obtained by matching the grey-scale porosity values to colors (Sammaljärvi, 2017). The resulting color map can highlight the local variations in porosities.

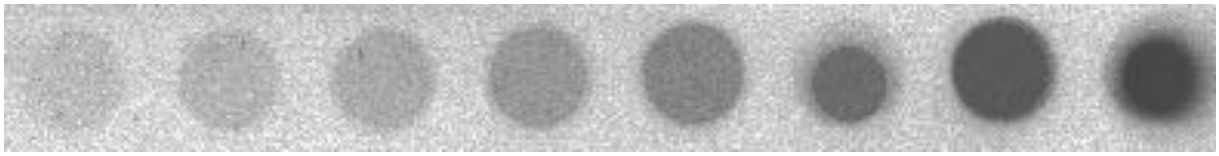

Figure 8. A calibration standard series with known activities (lower activities on the left, higher activities on the right)

An AG based on digital imaging plate requires a slightly different image processing procedure. In the plate, the beta radiation interacts with the europium-bromine-phosphor complex, resulting its excitation to a higher energy state (Sardini et al., 2015). The relaxation of the excited state with laser releases blue light with a specific wavelength. The local activity corresponds to the amount of blue light produced by a given location. The blue light is directed through an amplification tube to an analogue-digital converter. The converter inputs the digitized values into computer and the product is a 16-bit image (Sammaljärvi, 2017; Sardini et al., 2015). For digital image plates, the optical densities are calculated with equation **4.** (Sardini et al., 2015),

$$OD = OD_0' * A^{k'} \qquad \text{(Eq. 4.)}$$

where OD is the optical density for activity of 1 Bq/ml, A is the local activity and k' the fitting coefficient. The local activity A can be obtained by converting equation **4.** into equation **5.**

$$A = \left(\frac{OD}{OD_0'}\right)^{\frac{1}{k'}} \qquad \text{(Eq. 5.)}$$

The resulting activity values can be placed into equation **3.** to calculate porosities from digital image optical densities or by converting directly from grey values into activities with the standard series. For quantitative analysis, the 16-bit image using digital imaging plate produces smaller uncertainties. In film AG, the errors increase towards very high and very low grey values (Sammaljärvi, 2017).

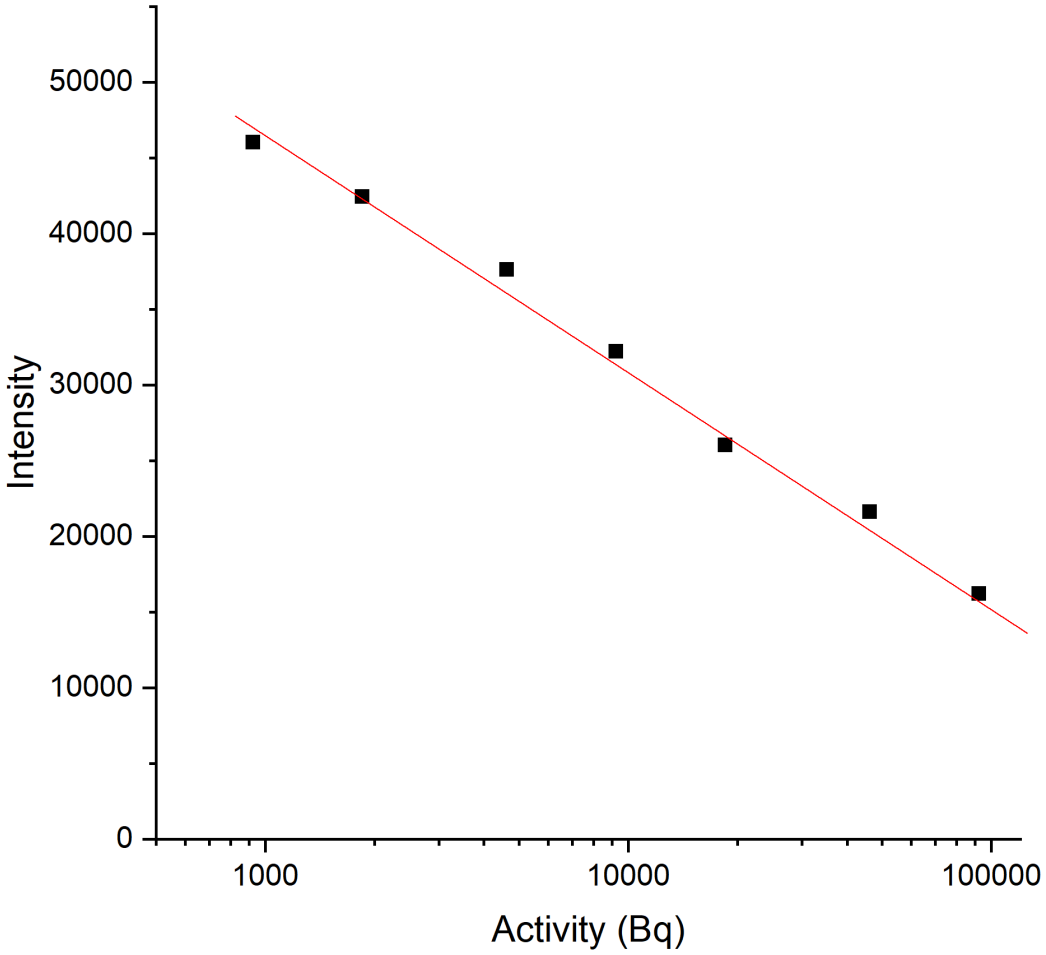

Figure 9. A calibration curve for digital autoradiography (16-bit image). The intensity is expressed as grey values. Each spot represents respective activity in the calibration series in Figure **8.**

3.5. Scanning electron microscopy with Energy dispersive elemental analysis

Scanning electron microscopy (SEM) produces image of a sample using a focused beam of electrons. The electrons are deflected from the surface of a sample or which detach secondary electrons from the sample structure (Friel, 2003; Lloyd, 1987) Secondary electrons (SE) provide information about the morphology of the sample. Backscattering electrons can be used to separate different phases with differing densities. This can be used to highlight minerals in the sample material. Energy dispersive X-ray analysis (EDS) can be combined with SEM to provide elemental analysis to confirm different mineral phases. EDS is based on an electron with certain energy hitting the shell of an atom, it can push an electron from the shell away (Friel, 2003). Outer shell electron will replace the remaining gap and decrease its

energy state. The result is a characteristic X-ray emission that can be detected in the EDS-detector.

The element distribution in the samples was studied with a Scanning Electron Microscope with Energy Dispersive X-ray spectroscopy (SEM-EDS). The analyses were performed with a JEOL TM JSM-7100F Field Emission Scanning Electron Microscope with Oxford Instruments Inca X-sight EDS system at the Geological Survey of Finland (GTK), with accelerating voltage of 20 kV. Furthermore, the SEM analyses were done with the Backscatter Electron imaging mode (BSE) to highlight the different elemental compositions of mineral phases. Finally, mineral identification was achieved by combining BSE image together with EDS analysis and comparing them with known literature values of distinguished minerals.

3.6. X-ray diffraction

X-ray powder diffraction (XRD) is used in characterizing crystalline structure and mineralogy of the material. X-rays are produced in an X-ray tube, where the high voltage maintained across the electrodes draws electrons toward a metal target (the anode). Characteristic x-rays are produced at the point of impact and radiate in all directions. A tube with copper target, which produces their strongest characteristic radiation (Kα1, wavelength ~1.5 Å), is used commonly (Poppe et al., 2001). In this work, a cobalt target is used instead. Cobalt produces longer characteristic wavelengths (~1.8 Å) and provides better peak separation at low-angle peaks (e.g. clay minerals) (Moore and Reynolds, 1997). When the incident x-ray beam hits a crystalline lattice, it is scattered although most of the scattering is interfered with destructive interference. If the scattering with certain direction is in phase with scattered rays from other atomic planes, they can mutually enhance each other by constructive interference, leading to diffraction. The diffraction follows Bragg's law (Equation **6.**) and its basics are presented in the Figure **10.** Each characteristic material with a crystalline structure has a unique atomic structure. Therefore, it will diffract X-rays in a distinguishable pattern.

$$n\lambda = 2d \sin\theta \qquad \text{(Eq. 6.)}$$

The XRD measurements were performed with Panalytical X'pert Pro MPD (2MB) diffractometer with a Cobalt anode (6.9 keV) in Institut de minéralogie, de physique de

matériaux et de cosmochimie (IMPMC) at Sorbonné University, Paris. The power used in scans was 1.6 kW (40kV generator voltage and 40mA tube current). The clay mineral identifications was achieved with the position of (001) reflections of the X-ray diffractograms (Moore and Reynolds, 1997).

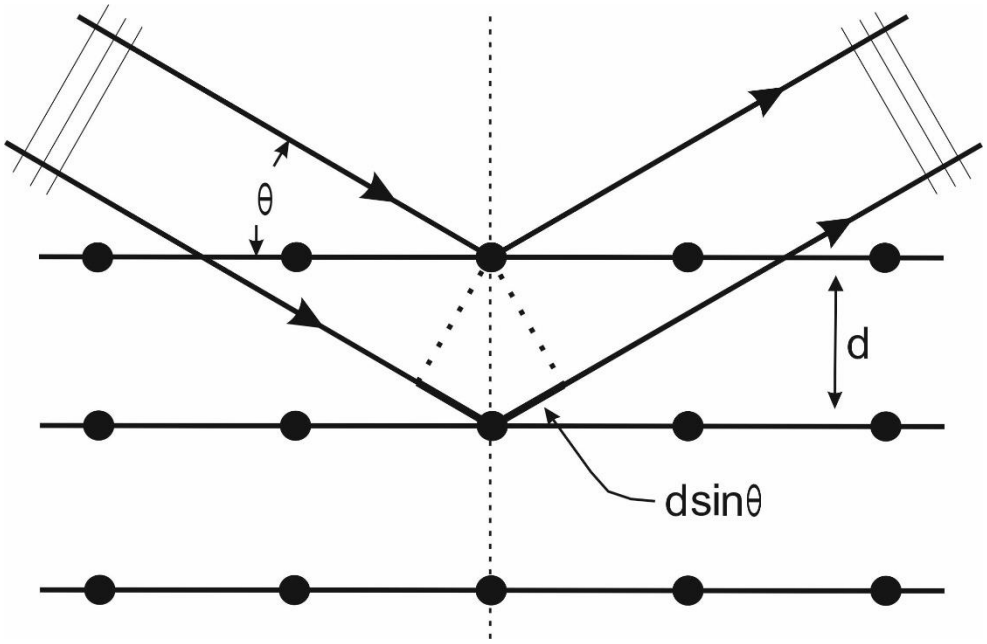

Figure 10. Bragg diffraction. The incident X-rays diffract from the plane lattice. The angle of scatter is denoted as 2θ.

Additionally, illite crystallinity was determined using the Kübler index. The Kübler index (KI) is the the full width at half-maximum height (FWHM) of the illite 10-Å X-ray diffraction peak (Kübler, 1964) and is measured from clay-fraction of an air-dried sample. KI is expressed as Δ°2θ and is commonly used as a measurement of illite crystallinity and metamorphic indicator at low-grade metamorphic facies (Jaboyedoff et al., 2001). The KI value decreases with increasing metamorphic grade, since the illite peak becomes narrower due to thickening of illite crystals in prograde metapelitic sequences (Abad, 2007). Figure **11.** presents the basics of KI determination based on the FWHM.

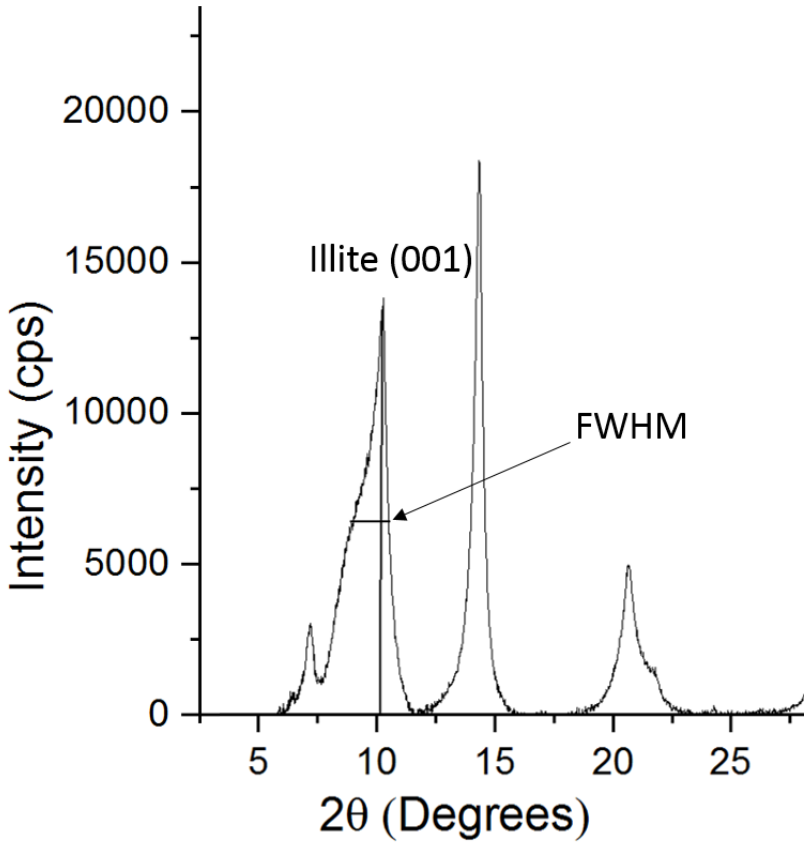

Figure 11. Kübler index (FWHM) for illite (001) peak from XRD-powder diffraction.

4. RESULTS

4.1. Fault core structure

The observed fault zone (F2) apparently exhibits more complex structure than presented in previous studies (Lefèvre et al., 2016; Dick et al., 2016). The eastern compartment of the FC is an area with slightly S-SSW dipping cleavage preserving slightly brecciated rock but without gouges. The fault core zone is in fact a 30 – 50 cm thick band that coincides with penetrative sub-vertical foliation structures and is located on the western side of the previously called FC zone (Nenonen et al., 2018). The fractures observed from the samples indicate coincide with brittle shear zones and associated riedel structures. The deformation structures observed on these structures indicates left-lateral movement that coincides with the last Pyrenean orogenic event (Lefèvre et al., 2016; Constantin et al., 2004). The fault gouges are distinguishable by

their dark color. Respectively, breccias and protolith surrounding gouges are lighter in color. This color disparity may indicate mineralogical differences between gouges and adjacent lithologies.

The fault gouge zone within the fault core is 30 – 50 cm wide section on the western side of the previously called fault core, next to the protolith. The fractures observed from the samples indicate riedel-structures and brittle shearing (Figure **12.**).

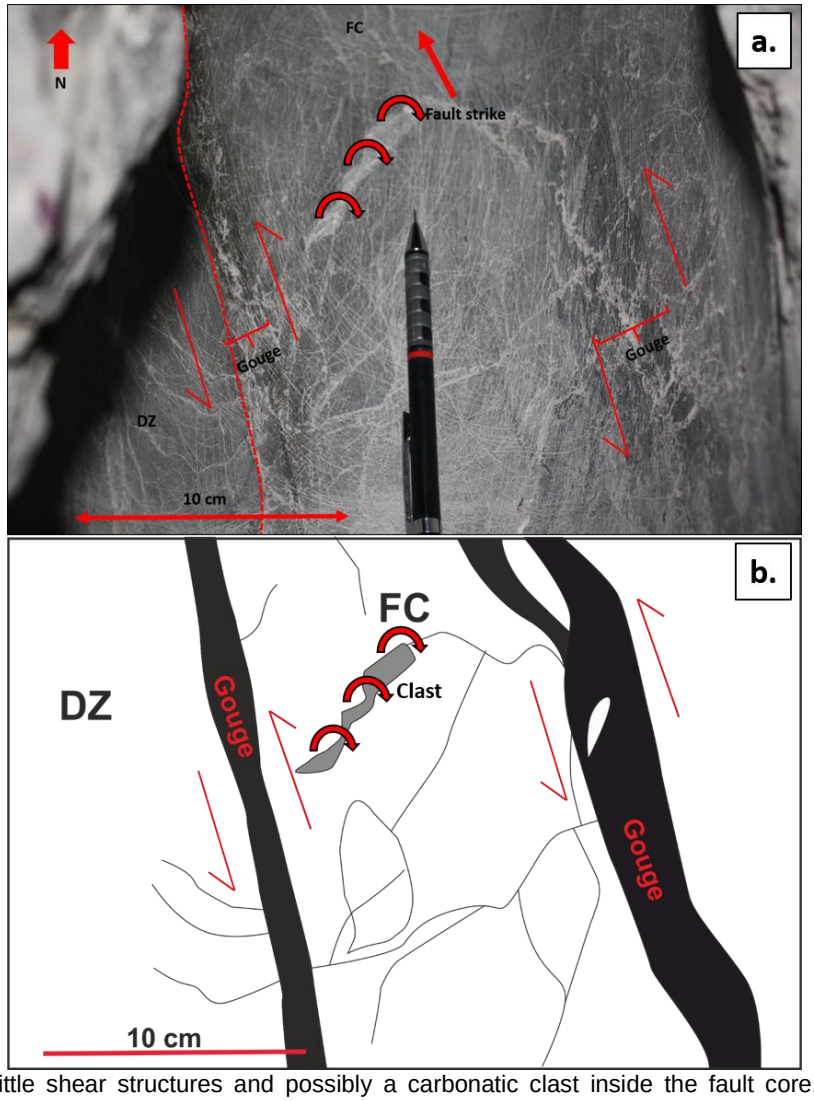

Figure 12. Brittle shear structures and possibly a carbonatic clast inside the fault core. The clast orientation indicates rotation according to sinistral shearing, which is coherent with the last Pyrenean compressive event (Lefèvre et al. 2016). **a.**: A photograph from fault core hole bottom. **b.**: a schematic of the fault core, damage zone and adjacent two gouges.

4.2. Optical microscopy from C-14-PMMA impregnated thin sections

The optical microscopy was performed on two thin sections, TS1 and TS3, which display Gouge 1 and Gouge 2 (Figure **13.**). Thin sections were observed and photographed with both plane- and cross-polarized light. Especially shear indicators and deformation structures were under interest.

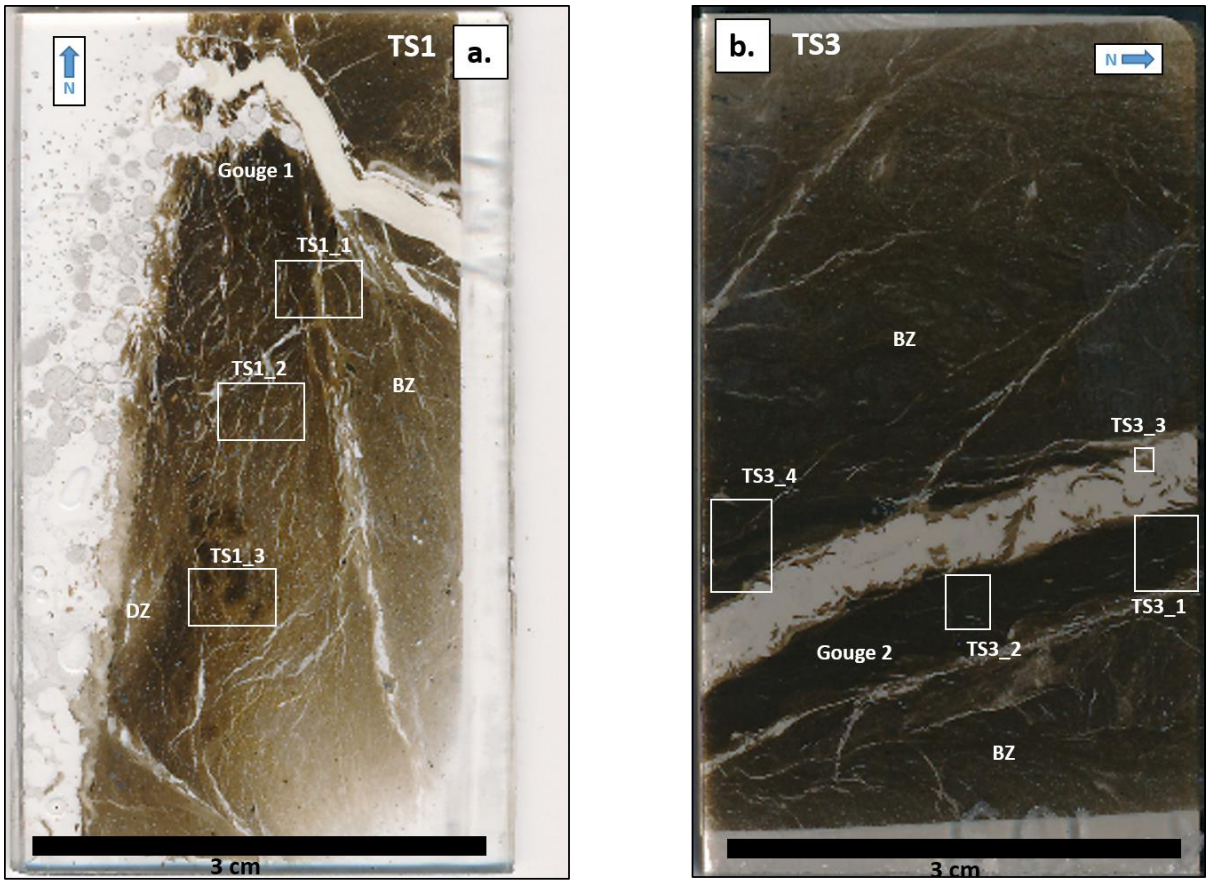

Figure 13. Table top scans of thin sections TS1 **a.** and TS3 **b.** TS1_1 is located on the interface between the brecciated zone and the Gouge 1, TS1_2 and TS1_3 are from the centre of the Gouge 1. TS3_1 and TS3_2 are from the centre of Gouge 2 and TS3_3 from the Gouge 2 and BZ interface.

The Gouge 1 displays different colours than the adjacent brecciated zone, which indicates mineralogical change between the two domains. Gouge 1 has more reddish colouring under crossed polars and contains shear deformation structures, such as R- and P-foliations (Figures **14**. and **16.**). Moreover, calcite is abundant on the BZ side (Figures **14**. and **15.**) but is absent inside the gouge. Calcite crystal in Figure **15.** is deformed with a sense of shear, indicating a co-seismic precipitation. Figure **14.** displays a set of photomicrographs from a narrow, sub-millimetric zone between Gouge 1 and the BZ. In this zone, clasts of quartz are within a clay-rich matrix. Foliations patterns could not be clearly observed inside the zone. It additionally

appeared with lighter colouring from the surroundings. The central area of Gouge 1 contains brittle-shear structures, most notably R-, P- and Y-shears (Figure **16.**). The sheared areas exhibit dark foliations which could indicate pressure dissolutions processes with more soluble minerals dissolving and insoluble mineral enrichment within the zone.

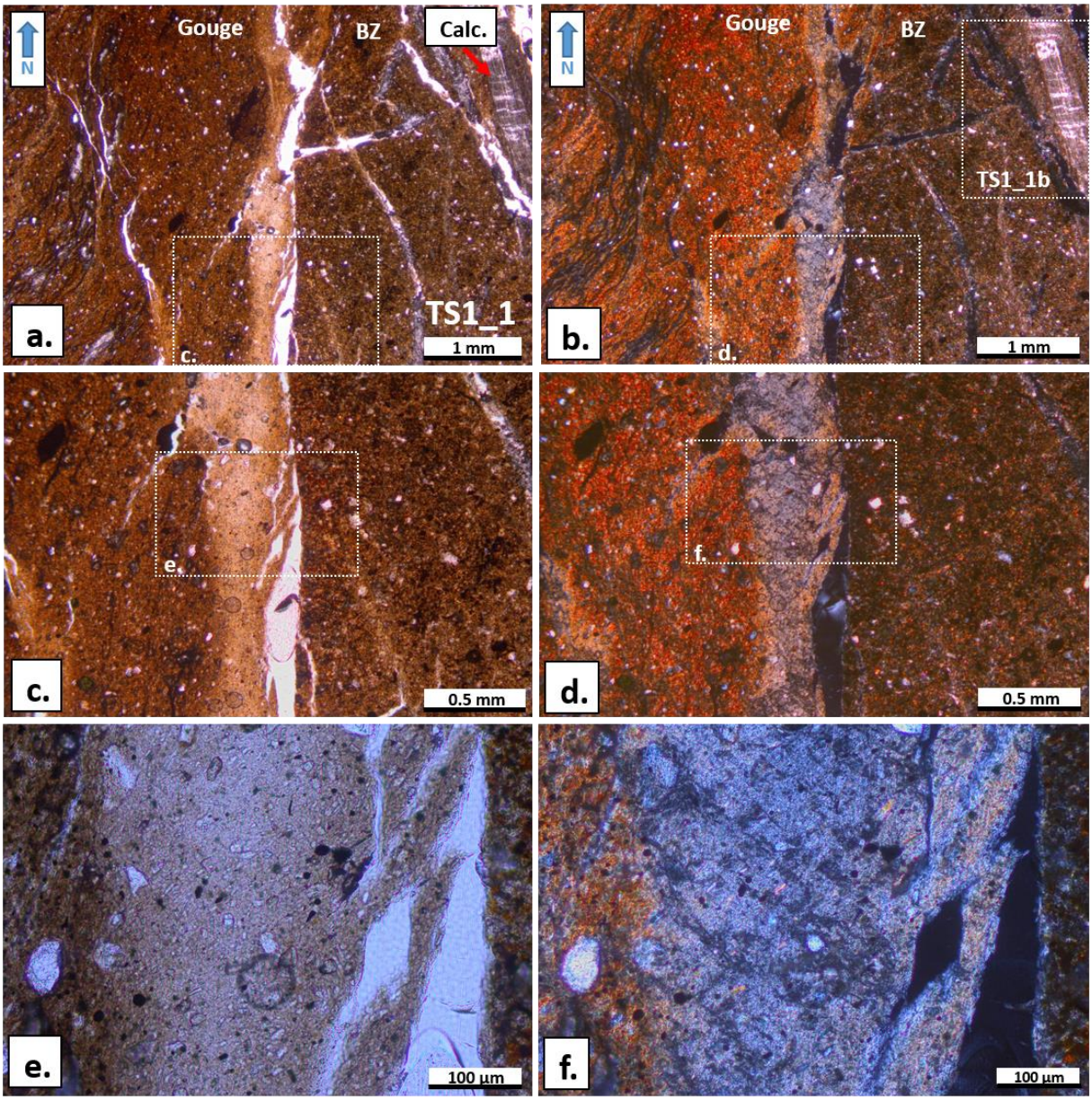

Figure 14. TS1_1 optical microscopy photographs. TS1_1 exhibits a gouge BZ interface. **a.**: Gouge 1 and BZ interface with plane polarized light. A crack filled with fibrous calcite (Cal.) is indicated by an arrow. **b.**: Gouge 1-BZ interface with cross-polarized light. **c.**: Greater magnification from the interface with plane polarized light. **d.**: Interface with cross-polarized light. **e.**: Area with lighter, isotropic gouge. Plane polarized light. **f.**: Isotropic gouge with cross-polarized light.

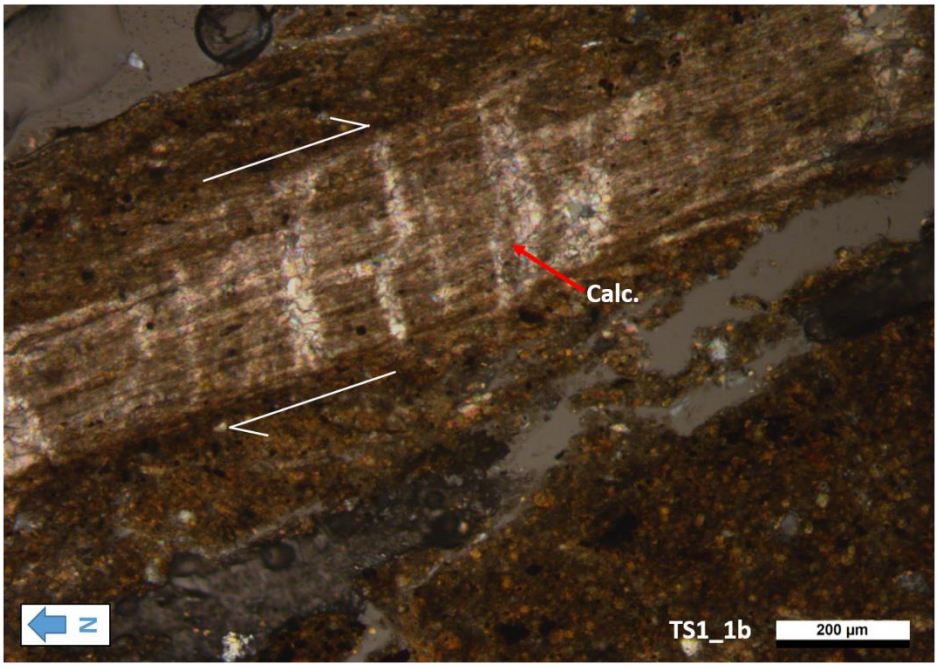

Figure 15. A micrograph of a fibrous calcite from TS1_1, inside the BZ. The fibrous calcite has been deformed and twinned by gliding, indicating syntectonic calcite formation and episodic calcite crack sealing. The shear sense (dextral in this case) can be observed from the calcite deformation structure.

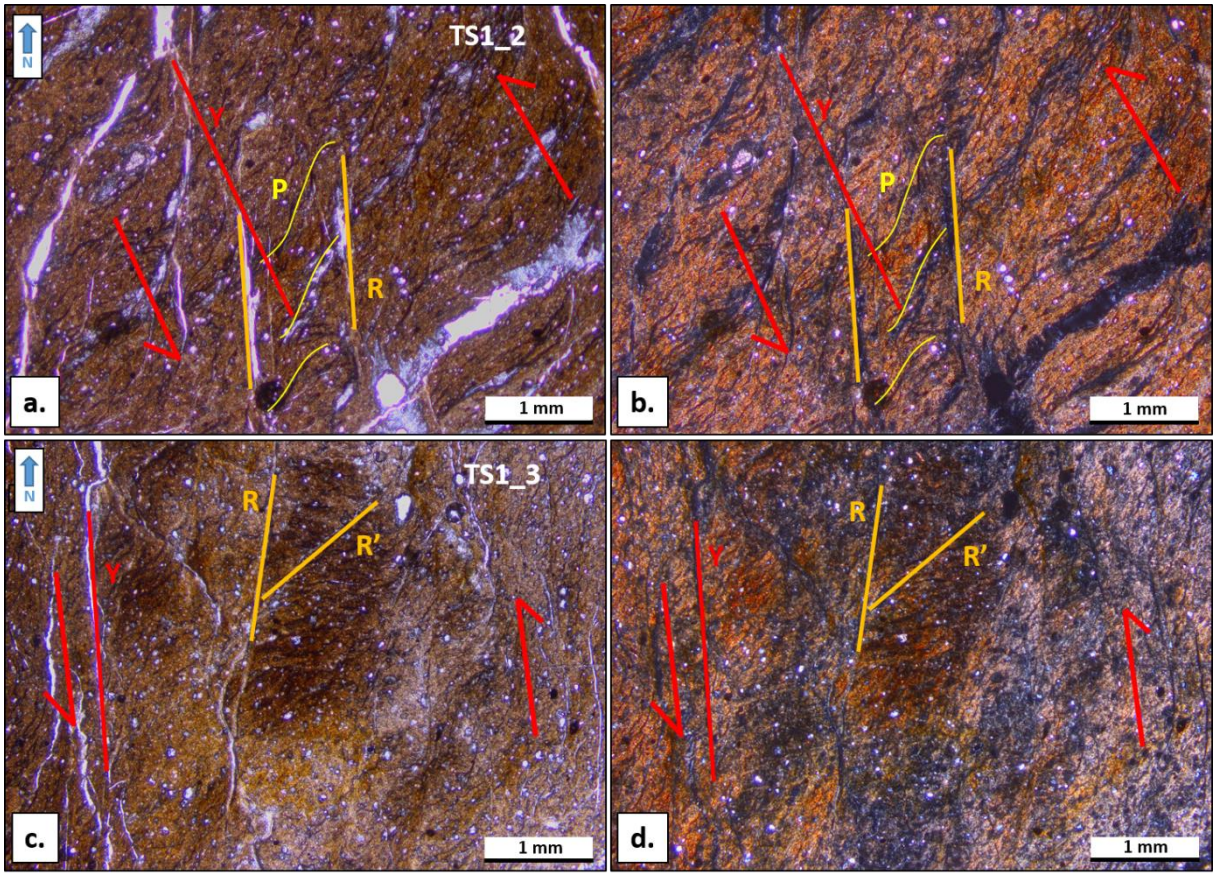

Figure 16. TS1 thin section micrographs taken under plane- and cross-polarized light. Micrographs from the central area of the Gouge 1. The structures in **a.** indicate high shear deformation with Riedel shears (R), Y and P-foliations. Dark bands are pressure dissolution seams. **b.**: TS1_2 with crossed polars. **c.**: TS1_3 with plane-polars. Similar structures than in **a.** can be observed with sinsitral sense of shear. **d.**: TS1_3 with crossed polars.

Gouge 2 photomicrographs (TS3, Figure **17.**), reveal a lesser deformed gouge area than found in the Gouge 1. Only R-shears and adjacent pressure dissolution areas could be observed. Furthermore, Gouge 2 contains a similar narrow zone of lighter colouring (Figure **18.**) than in Gouge 1. The photomicrograph displays a sign of weak flow and grain rotation in the clay matrix. Generally, Gouge 1 exhibits stronger shear deformation structures than Gouge 2.

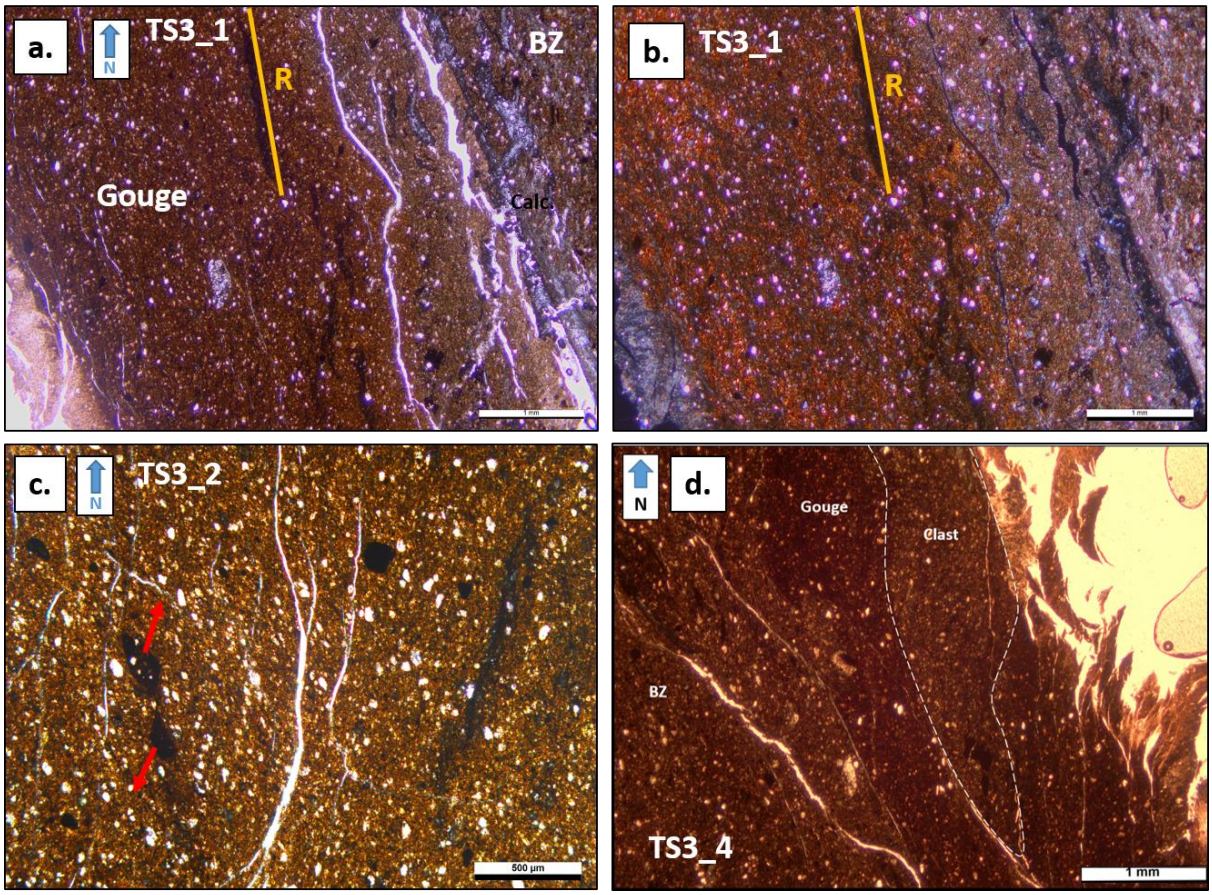

Figure 17. Photomicrographs from the TS3. **a.**: TS3_1 in plane-polarized light. Figure **b.**: TS3_1 with crossed polars. **c.**: TS3_2 with plane-polarized light. Red arrows indicate a fractured grain with a sense of shear. **d.**: TS3_4 with plane-polarized light. Dashed line indicates a carbonatic clast incorporated into gouge from the BZ.

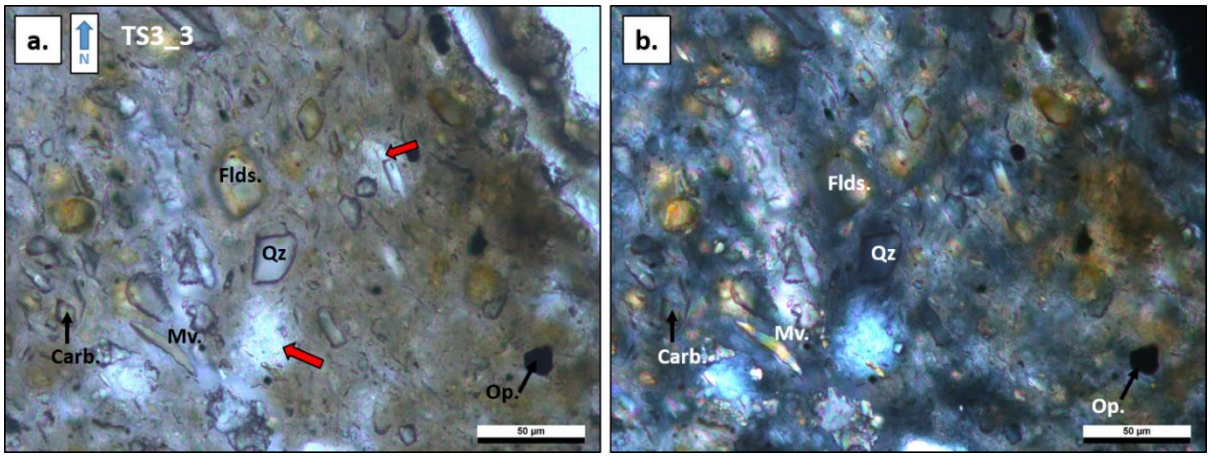

Figure 18. **a.**: TS3_3 with plane-polarized light. **b.**: TS3_3 with crossed polars. Red arrows in **a.** point empty pore spaces. Grains are quartz (Qz), feldspars (Flds.), muscovite (Mv.), opaques (Op.) and carbonates (Carb.) in a fine-grained clay-matrix.

4.3. C-14-PMMA autoradiographs

The ^{14}C-PMMA autoradiographs (AG) from the samples indicate significant variations through the gouge and adjacent breccias and damage zone. The central gouge displays porosity values approaching to undeformed protolith (11 %, Dick et al., 2016), but still considerably higher (15 – 20 %) in both Gouges 1 and 2. However, in the margins of the gouge, the porosity values increase to 30 – 60 % (Nenonen et al., 2018). A previous study has demonstrated an ascent in porosity along the damaged zone using gravimetric methods (Lefèvre et al., 2016). This bulk measurement did not reveal the changes in gouge porosity however. The AG on the other hand allows the determination of exact locations of increased porosities, which cannot be achieved with conventional porosity methods.

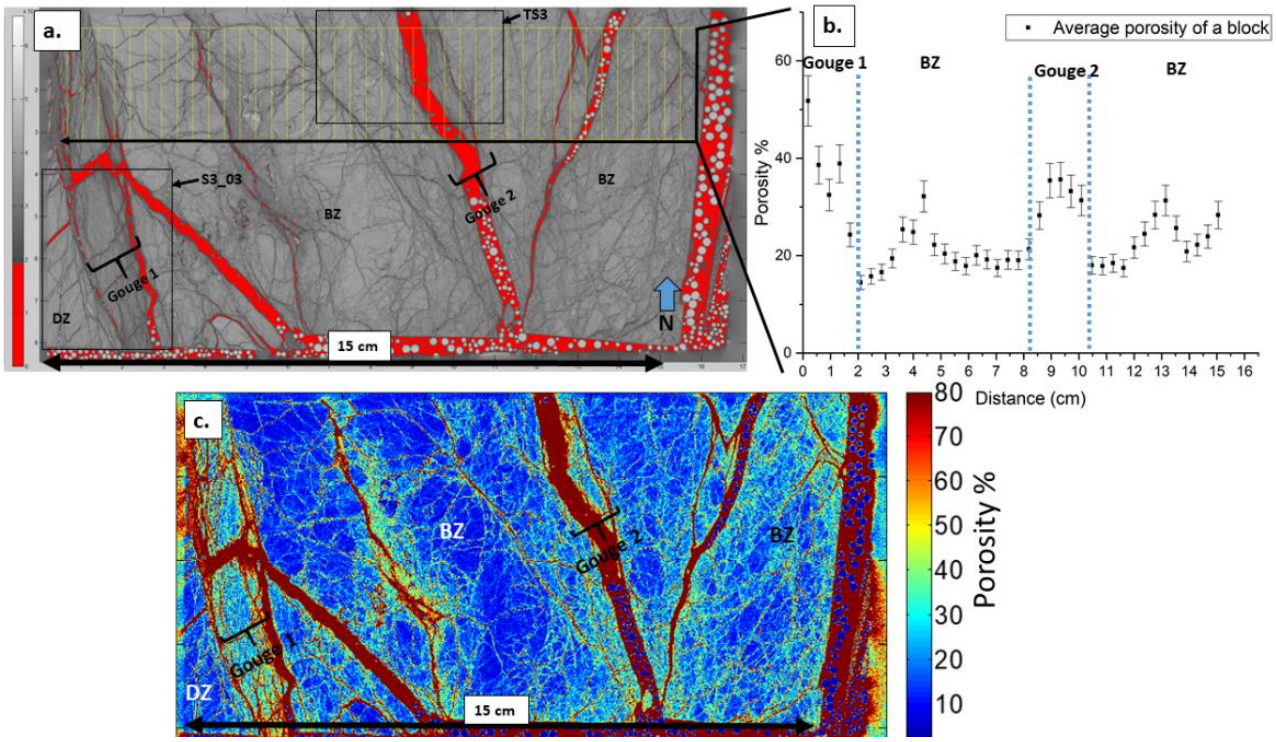

Figure 19. AG porosity map from the polished surface of S3. **a**.: The darker grey values indicate higher PMMA intensities and therefore higher porosities and lighter values have lower intensities and lower porosities. Yellow rectangle with sections represents a porosity profile across the S3 surface. The red areas are fractures with pure PMMA (excavation and sample handling artefacts). Grey values representing pure PMMA values are thus excluded from porosity calculations. Spheres inside the PMMA are from the epoxy resin. Samples S3_03 and TS3 are indicated by rectangles. **b.**: a porosity histogram from the block profile of **a.** An average porosity of each block of the yellow rectangle is represented by a dot with error values. Gouge 1, gouge 2 and brecciated zones (BZ) are distinguishable in the porosity map **a.** as different grey levels.
c.: A colour map of porosity of S3 with porosity range of 0 – 80%.

Gouges appear to have higher intensities as they exhibit darker grey values than the surrounding DZ and BZ. It can be assumed that the gouges have thus higher porosities. The porosity histogram (**18 b.**) further indicates that the gouges are distinguishable from the adjacent zones. Gouge 1 appears to exhibit porosity values as high as 40 %. Respectively, in gouge 2 porosity values approach to at least 35 %. The brecciated zones appear to have a wide range of porosities from ~13 % to ~30 %. Lowest porosities appear close to gouges. The colour map of porosity in S3 (Figure **18 c.**) further shows the heterogeneity in terms of porosity along the fault core. The BZ appears more homogeneous and with lower porosity than the gouges. The BZ is crosscut by possibly co-seismic shear fractures however. These fractures exhibit higher porosities than the bulk of the breccia.

Closer observation on the Gouge 1 reveals a spatial difference of porosity within the gouge (Nenonen et al., 2018) (Figure **20.**). The porosity values in the DZ are below 20 % but increase significantly up to 40 – 50 % in the Gouge 1-DZ interface. Porosity values decrease towards the

central gouge and approach to the values of DZ. The porosity increases again on the Gouge 1-BZ boundary.

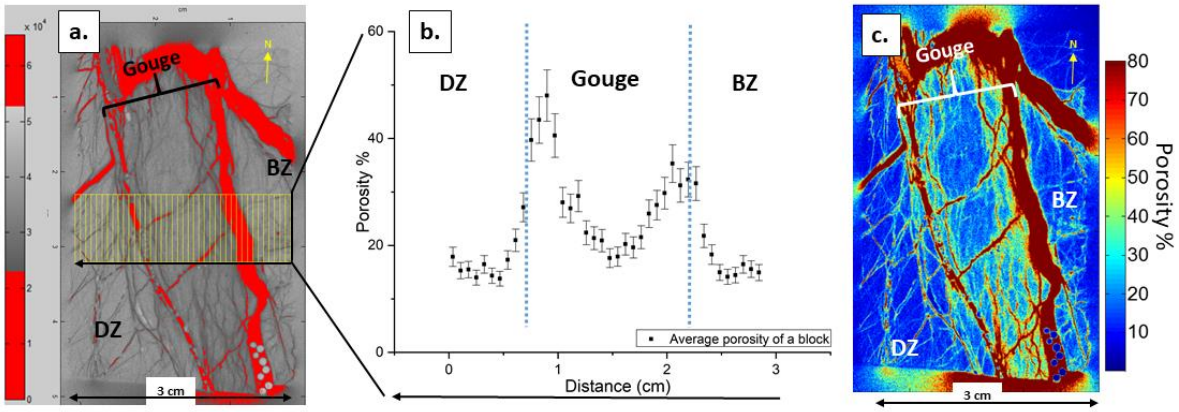

Figure 20. The AG porosity map of S3_03 and Gouge 1. **a.**: the AG with red areas that were excluded from the porosity calculations. **b.**: a block profile representing the yellow rectangle in **a.** The average porosity of each block is represented as a point with error values. **c.**: a colour map of porosity in S3_03 with porosity range of 0 - 80%.

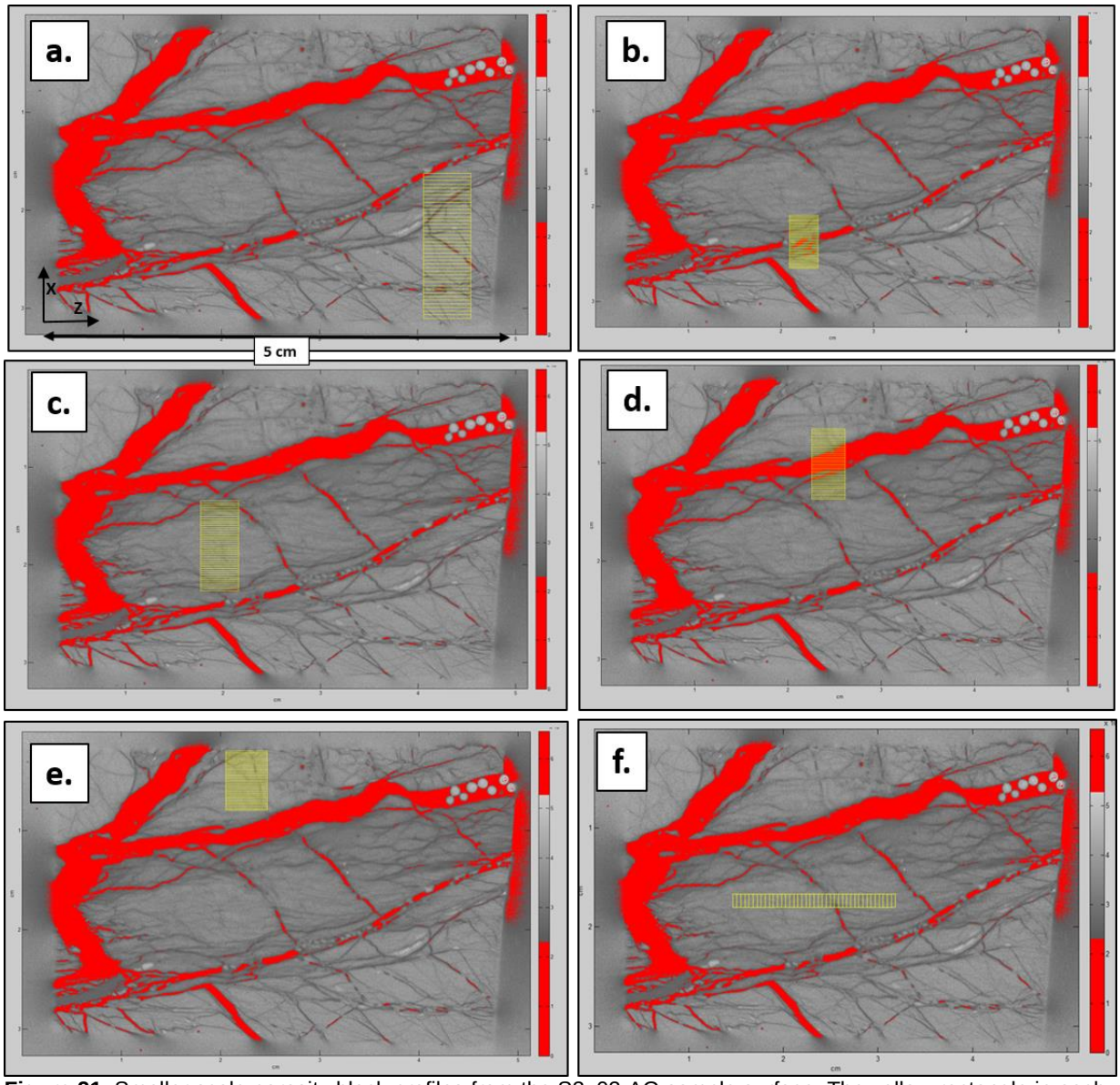

Figure 21. Smaller scale porosity block profiles from the S3_03 AG sample surface. The yellow rectangle in each figure represents the profile area illustrated as a porosity diagram in the figure **22.** The letters in **21.** and **22.** are consistent and each figure represents corresponding letter in the porosity diagram in the Figure **22**. **a.** is from the DZ, **b.** from the gouge-DZ interface, **c.** from the centre of the gouge, **d.** from the gouge-BZ interface, **e.** from the BZ and **f.** is a profile along the gouge centre.

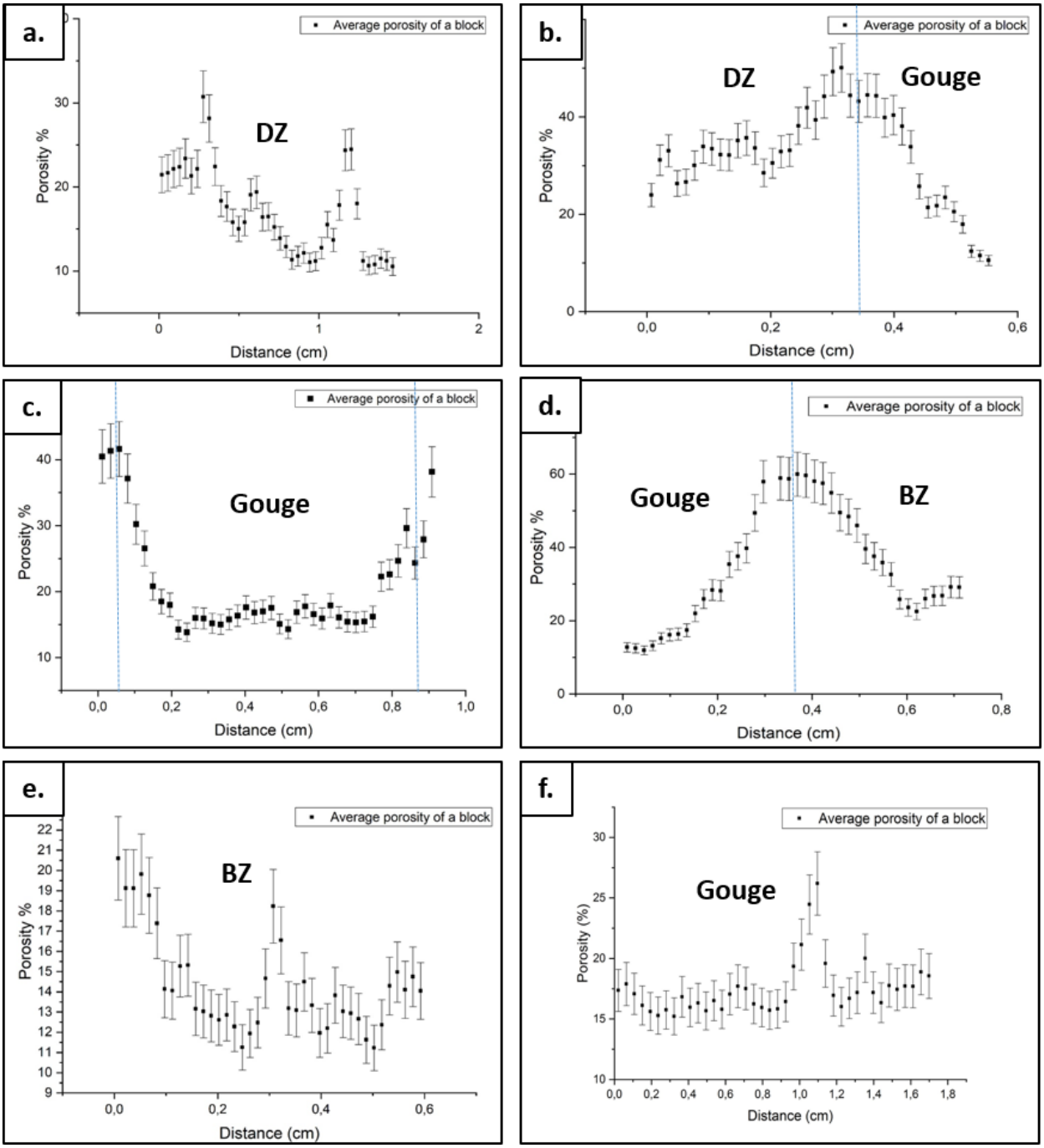

Figure 22. The porosity diagrams from the profiles of the sample S3_03, from the previous Figure **21.** Dashed blue lines indicate interfaces between domains. **a.**: The porosity profile of the damage zone (DZ). **b.**: The porosity profile of the DZ-Gouge 1 interface. **c.**: The porosity profile of the Gouge 1 interior. **d.**: The porosity profile of the Gouge 1-Western BZ interface. **e.**: The porosity profile of the Western BZ. **f.**: Porosity profile taken parallel along the fault inside Gouge 1.

In Figure **22a**. porosity is heterogeneous and appears to diminish towards the gouge. Increasing porosity values appear to follow fractures. The DZ-gouge boundary (Figure **22b.**) exhibits an increase in porosity values on this zone, probably due to micro-fissuring. The highest values (~ 50 %), are on the gouge side of the DZ-gouge interface. Inside the interior gouge (Figure **22c.**) porosity values drop significantly after the high porosities of the DZ-gouge boundary. The

porosity values display a similar steep increase on the gouge-BZ boundary. In the gouge-BZ interface (Figure **22d.**) porosity increases up to ~60 % in a zone with width of 0.4 cm. The BZ (Figure **22e.**) contains porosity values approaching to undeformed Tournemire argillite. Figure **22f**. is a porosity profile taken parallel to the direction of shearing.

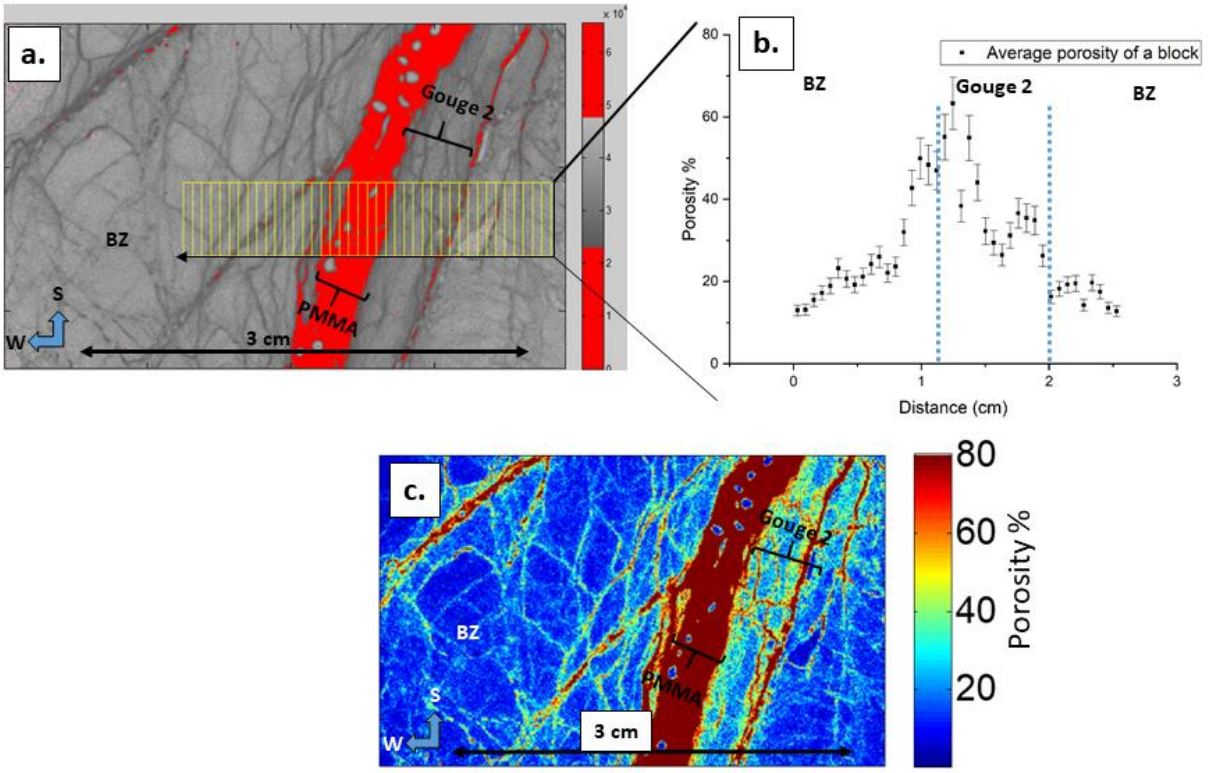

Figure 23. The AG porosity map of TS3. **a.**: the AG with red areas (pure PMMA) that were excluded from the porosity calculations. **b.**: the block profile from **a. c.**: the colour map of porosity in TS3 with porosity range of 0 – 80%.

Calcite fillings have lowest porosity and appear in Figure **23a.** as the lightest areas and in Figure **23 c.** as the darkest blue areas. The calcite crack-filling in Figure **22a.** can likewise be observed in porosity diagram **22b.** as a sudden drop in porosity when moving from the Gouge 2 into the right-sided BZ.

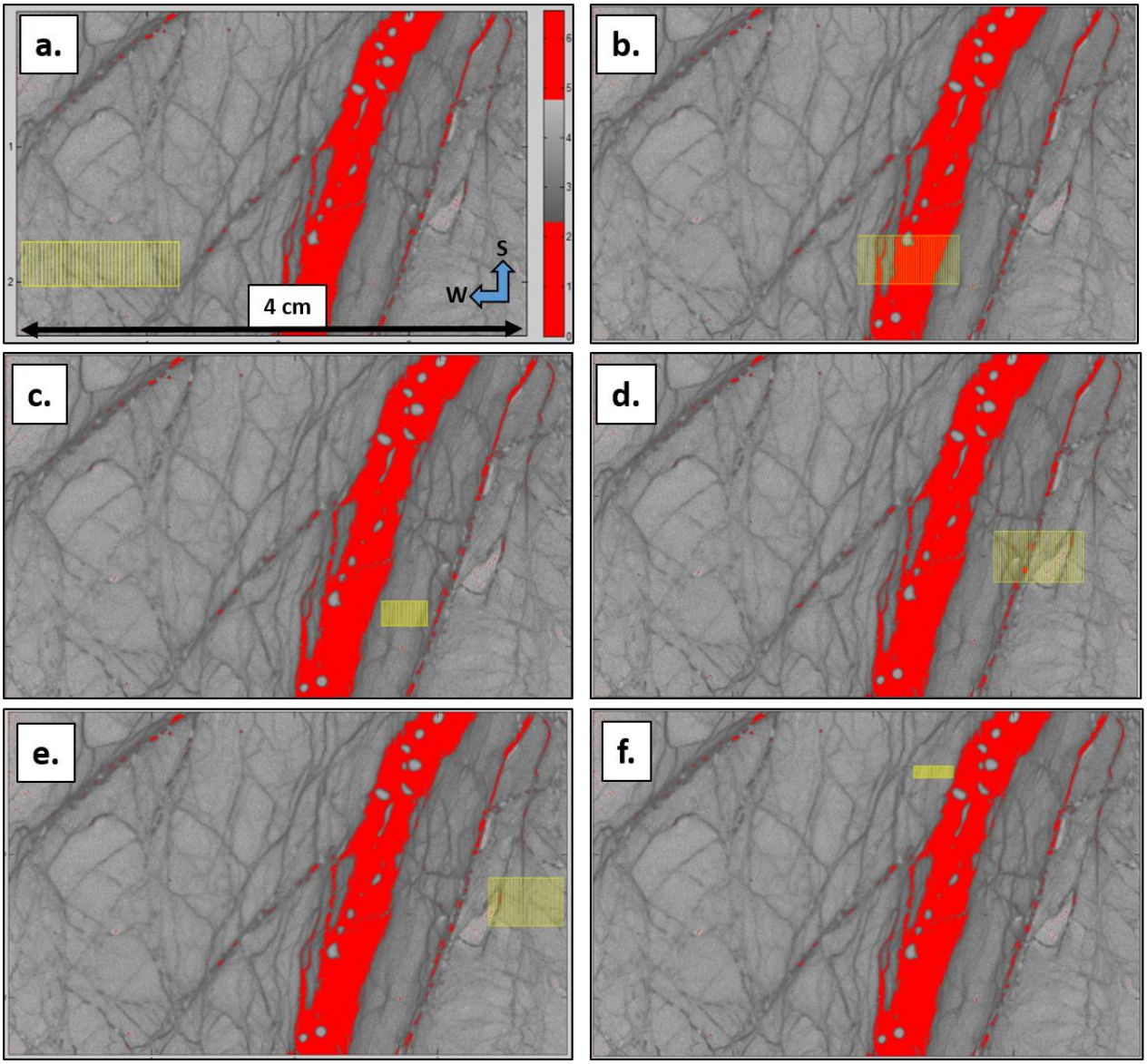

Figure 24. Smaller scale porosity block profiles from the TS3 sample surface. The yellow rectangle in each figure represents the profile area illustrated as a porosity diagram in the Figure **25**. The letters in Figures **24**. and **25**. are consistent and each figure represents corresponding letter in the porosity diagram in the Figure **24**. **a.** is from the BZ, **b.** from the BZ-gouge interface, **c.** from the centre of the gouge, **d.** from the gouge-BZ interface, **e.** from the BZ and **f.** is from the BZ with clasts inside gouge originating possibly from the host rock.

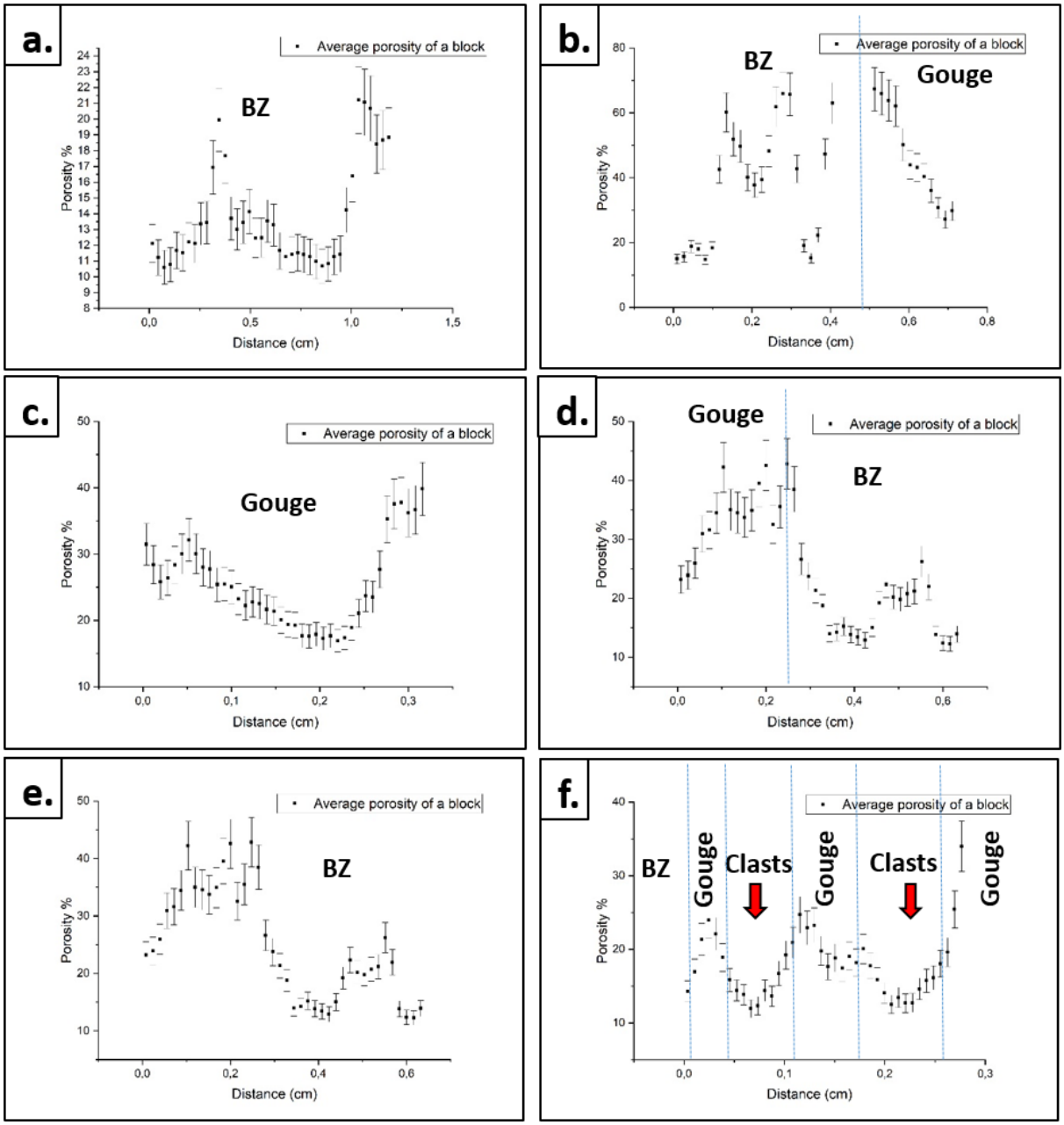

Figure 25. The porosity diagrams from the TS3 AG profiles (Figure **24.**). **a.**: Western BZ porosity profile. **b.**: The porosity profile of the Western BZ-Gouge 2 interface. **c.**: The porosity profile of the interior of Gouge 2. **d.**: The porosity profile of the Gouge 2-Eastern BZ interface. **e.**: The porosity profile of the Eastern BZ. **f.**: Western BZ-Gouge 2 interface with clast porosities indicated by red arrows.

In the BZ1 between Gouge 1 and 2, porosity increases in fractured areas and towards BZ1-Gouge 2 interface (Figure **25a.**). The interface of the BZ1 and Gouge 2 (Figure **25b.**) contains a wide range of porosities from below 20 % (calcite in the BZ) up to 60 % (high-porosity gouge). Profile from the central gouge (Figure **25c**.) has in the margin porosity values up to 30 % but they gradually decrease towards the lowest values in the central gouge. Porosity values increase steeply again on the gouge-BZ2 interface. The Gouge 2-BZ2 interface show porosity values of 40 % (Figure **25d.**). Porosity decreases significantly towards the BZ2 (to 10 – 15 %) and then rise to ~20 %, eventually decreasing again to 10 – 15 %. The breccia shows very

heterogeneous porosity along the profile (Figure **25e.**). A possible clast profile from the BZ1 side of the gouge can be observed from the AG porosity variations within the BZ1-Gouge 2 interface (Figure **25f.**). The clasts are probably originated from the breccia wall, which could indicate wall-rock rip-off during a seismic slip within a fault zone.

The porosities observed display significant variations across the gouges. One significant feature is, that the highest porosity areas coincide with the most fissured areas within the gouges. Thus, the larger porosities could mostly exist as micro-fissures. In Table **1.** is a summary of porosity results for each structural domain within the F2 fault core.

Table 1. AG porosity results from the F2 fault core. Error (~10 %) is from autoradiography (Sammaljärvi et al., 2012).

	Undeformed shale	DZ	Interior gouge	Gouge 1/DZ side	Gouge /BZ1 side	BZ 1	Gouge/ BZ 2 side	BZ 2
Gouge 1 Porosity %	11 (Dick et al., 2016).	16 (±2)	18 (±2)	30 (±3)	40 (±4)	18 (±2)		
Gouge 2 Porosity %			20 (±2)		50 (±5)	13 (±1)	35 (±4)	15 (±2)

4.4. XRD results

The bulk-XRD measurements from the whole-rock powder revealed that the major mineral assemblages are quartz, feldspar, carbonates (calcite, dolomite, ankerite), and phyllosilicate minerals, such as illite, kaolinite and chlorite. The bulk analysis did not reveal any significant changes along the fault core.

The clay-fraction (< 2µm) of the sample was estimated by semi-quantitative XRD method (Biscaye, 1965). The average relative percentage of illite and illite-smectite (I/S) interstratifications are ~ 40 % and 10 – 15 % respectively in the damaged zone and breccias. However, in the gouges the respective relational fractions are ~ 30 % and 0 – 5% respectively and thus displaying a significant drop in the I/S content (Figure **26**.). Similar development in the fault core clay mineralogy was noted in other studies (Moreno et al., 2018; Dick, et al.,

2016). In the same way, the fault gouge kaolinite content showed a higher content in the fault gouge (Figure **26.**). The brecciated zones have varying mineralogical composition, but they resemble the damaged zone in clay mineralogy.

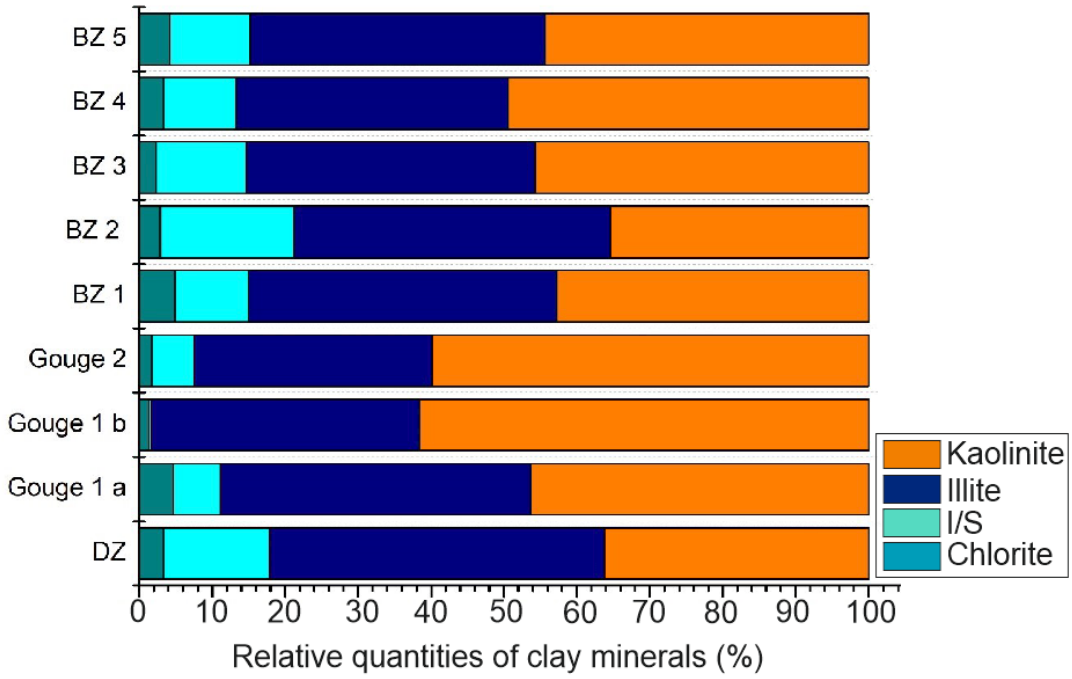

Figure 26. Relative quantities of clay minerals from XRD measurements of <2 µm fraction. Gouge 1 b sample location is from the high-porosity area on the Gouge 1 – BZ interface. Gouge 1 a is from the low-porosity central area of Gouge 1.

Additionally, Kübler indices (KI) were determined for illite crystallinities in different structural domains (Table **2.**). KI values for gouge samples varied between 0.44 and 0.78. Respective KI value for DZ was 1.34. Breccias expressed wide range of KI values ranging from 0.52 to 1.66.

Table 2. Illite crystallinity indices (Kübler index; KI) for each XRD sample.

XRD sample	KI (FWHM, Δ°2θ)
Gouge 1 a	0.47
Gouge 1 b	0.44
DZ	1.34
BZ1	0.52
BZ2	1.66
BZ3	1.27
Gouge 2	0.78
BZ4	0.63
BZ5	0.63

4.5. SEM-EDS results

Sample S3_03 and thin section TS3 surfaces were observed with SEM in secondary electron (SE) and BSE modes (Figures **27.**, **28.**, **29.**, and **30.**). SEM images were taken in BSE mode, as it highlights the different mineral densities. In addition, BSE images from the Gouge 1 and adjacent DZ and BZ in sample S3_03 display brittle-deformation structures, such as R- and R'-shears.

The SEM-EDS elemental mapping of the sample S3_03 revealed a zonation in the Gouge 1 (Figure **30.**) with iron forming concentration spheres around the central gouge (Nenonen et al., 2018). When compared to the porosity map from the AG (Figures **21.** and **22.**), iron is located along fractures and surrounds the lowest porosity area of the gouge. Potassium (Figure **29a.**) on the other hand is depleted from the interior of the gouge, but unlike iron, it does not follow the fractures. Nevertheless, potassium is concentrated on the high porosity areas within the gouge. Additionally, the eastern side of the gouge (brecciated zone) displays a lower content of potassium and higher of calcium (Figure **29c.**). The brecciated zone (BZ) therefore has more calcium carbonate content and less clay minerals (Nenonen et al., 2018). This could indicate a healing process on the BZ by crack-sealing (Lefèvre et al. 2016), with regards to the DZ and strengthening the fault more on its eastern side within the gouge. The Sulphur content on the other hand is generally more concentrated on the DZ as pyrite crystals (Figure **29b.**). However, it displays additional higher concentrations within the gouge centre. These sulphur-rich areas coincide with low-porosity areas within the gouge. The mineralogical findings and porosity results are tabulated in Table **3**.

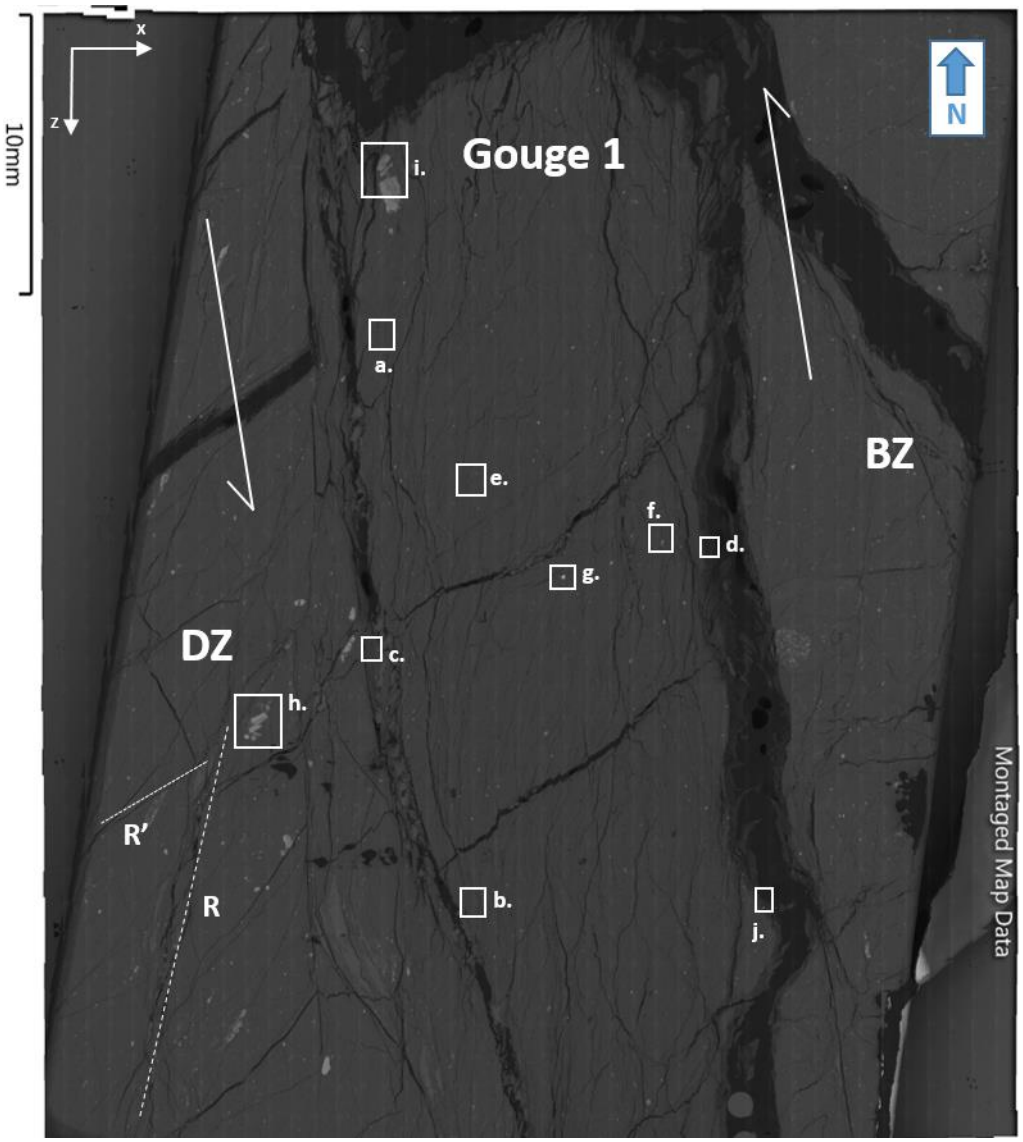

Figure 27. BSE image of S3_03 sample with smaller images in Figure **28**. with greater magnification marked with letters a.- j.

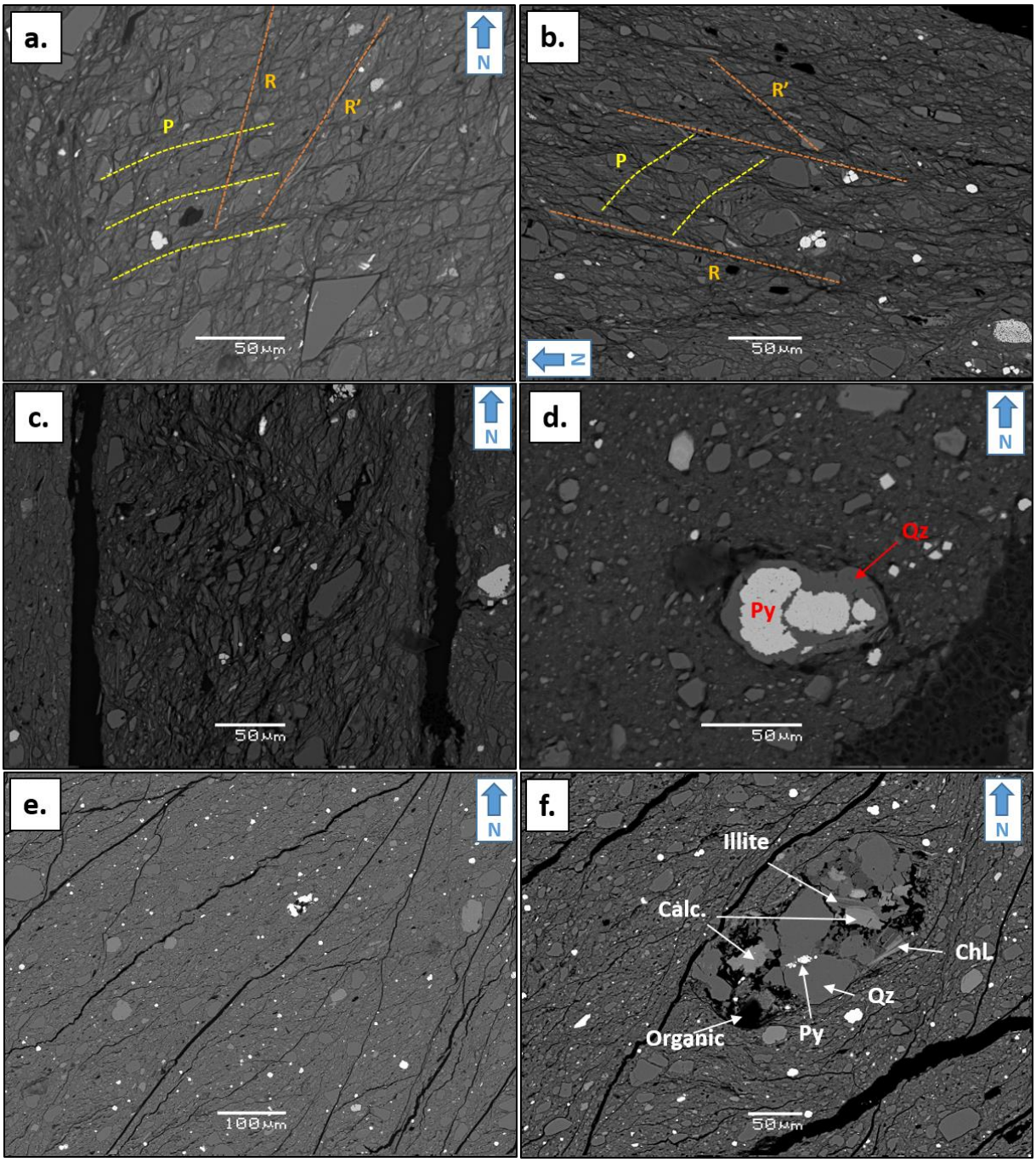
a.
R
R'
P
N
50µm
b.
R'
P
R
N
50µm
c.
N
50µm
d.
N
Qz
Py
50µm
e.
N
100µm
f.
N
Illite
Calc.
ChL
Qz
Py
Organic
50µm

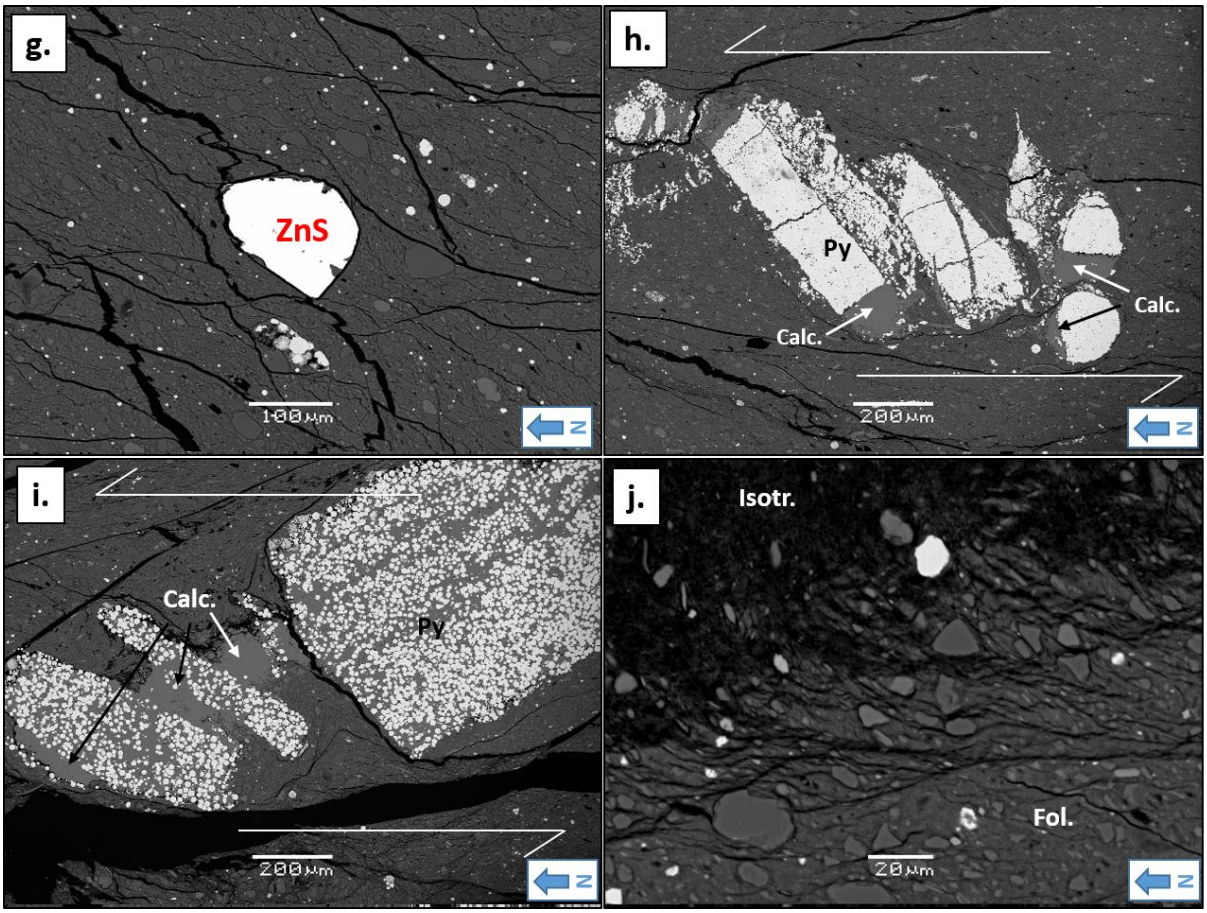

Figure 28. BSE image of the sample S3_03 surface. **a.** and **b.**: R-, and R'-shears and P-foliations in Gouge 1. **c.**: Foliation of a flow pattern close to the DZ boundary of Gouge 1. **d.**: Quartz-coated framboidal pyrite (Py) clasts close to the Gouge 1-BZ boundary. **e.**: Area of lower porosity central gouge. **f.**: A polymineralic, almond shaped clast on the BZ side of the Gouge 1. The clast contains Illite, calcite (Calc.), chlorite (Chl.), quartz (Qz), pyrite (Py) and organic material. **g.**: An authigenic sphalerite (ZnS) grain inside the Gouge 1. **h.**: A pyrite (Py) domino inside the DZ with rotation of the orientation of shearing with calcite (Calc.). **i.**: A pyrite (Py) domino inside the Gouge 1 with calcite (Calc.) between the rotated pyrite clasts. **j.**: Gouge 1 boundary between the foliated (Fol.) and isotropic (Isotr.) gouges.

SEM-EDS elemental mapping from sample S3_03 revealed grains of sphalerite within the Gouge 1 (Figure **30.**). Sphalerite grains were euhedral and thus most likely epigenetic and not detrital origin. Closer SEM-EDS observation from the iron zonation revealed that iron is mostly in clay-minerals as Fe-chlorite or chamosite (Figure **31.**). Chlorite grains appeared lighter from the illitic clay-matrix.

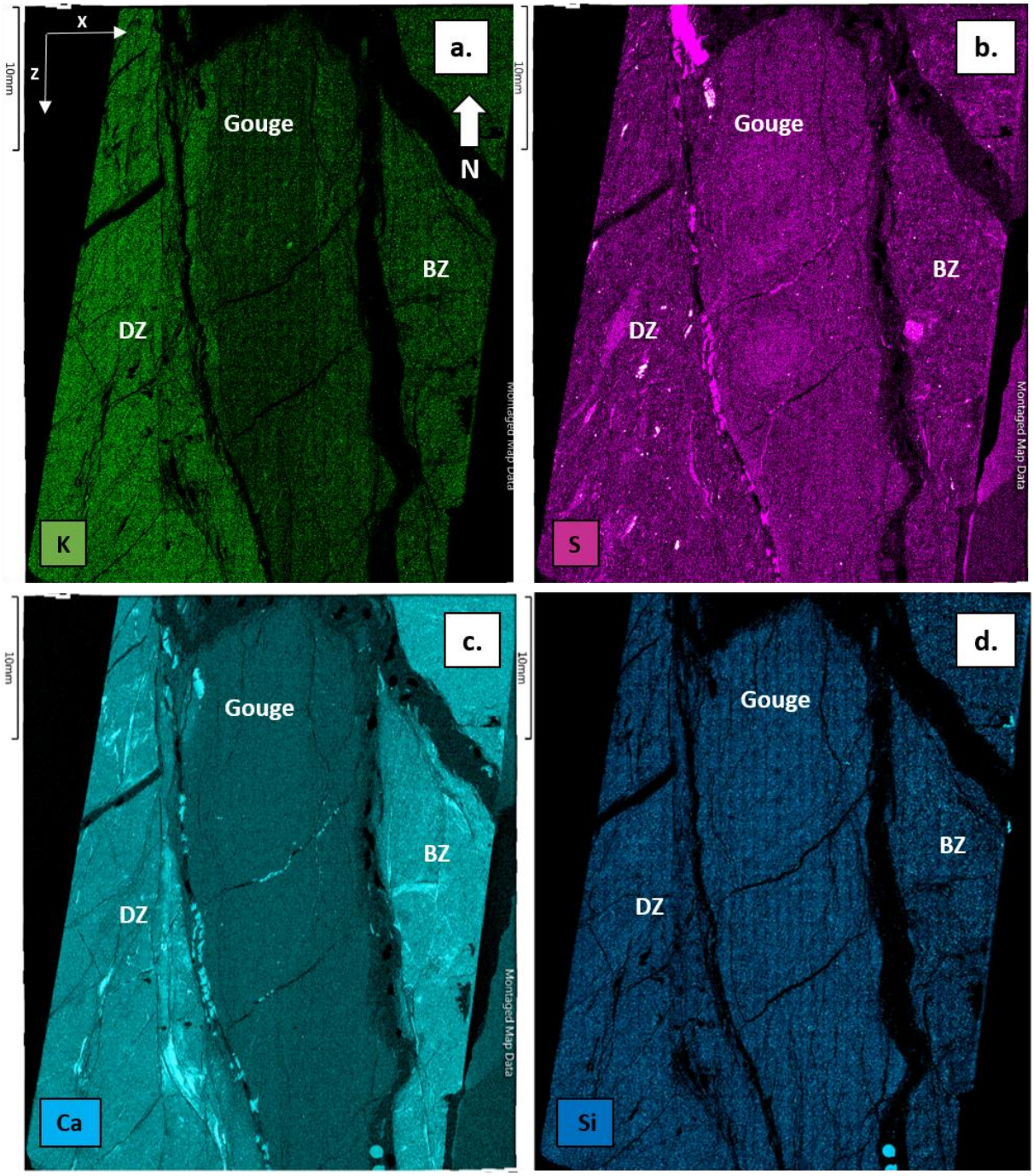

Figure 29. SEM-EDS elemental maps of the S3_03 sample. **a**.: Potassium displays higher concentrations on the DZ than inside the gouge or BZ. **b.**: Sulphur is generally more concentrated on the DZ. **c.**: Calcium is depleted in the gouge. **d.**: the silica content of the sample.

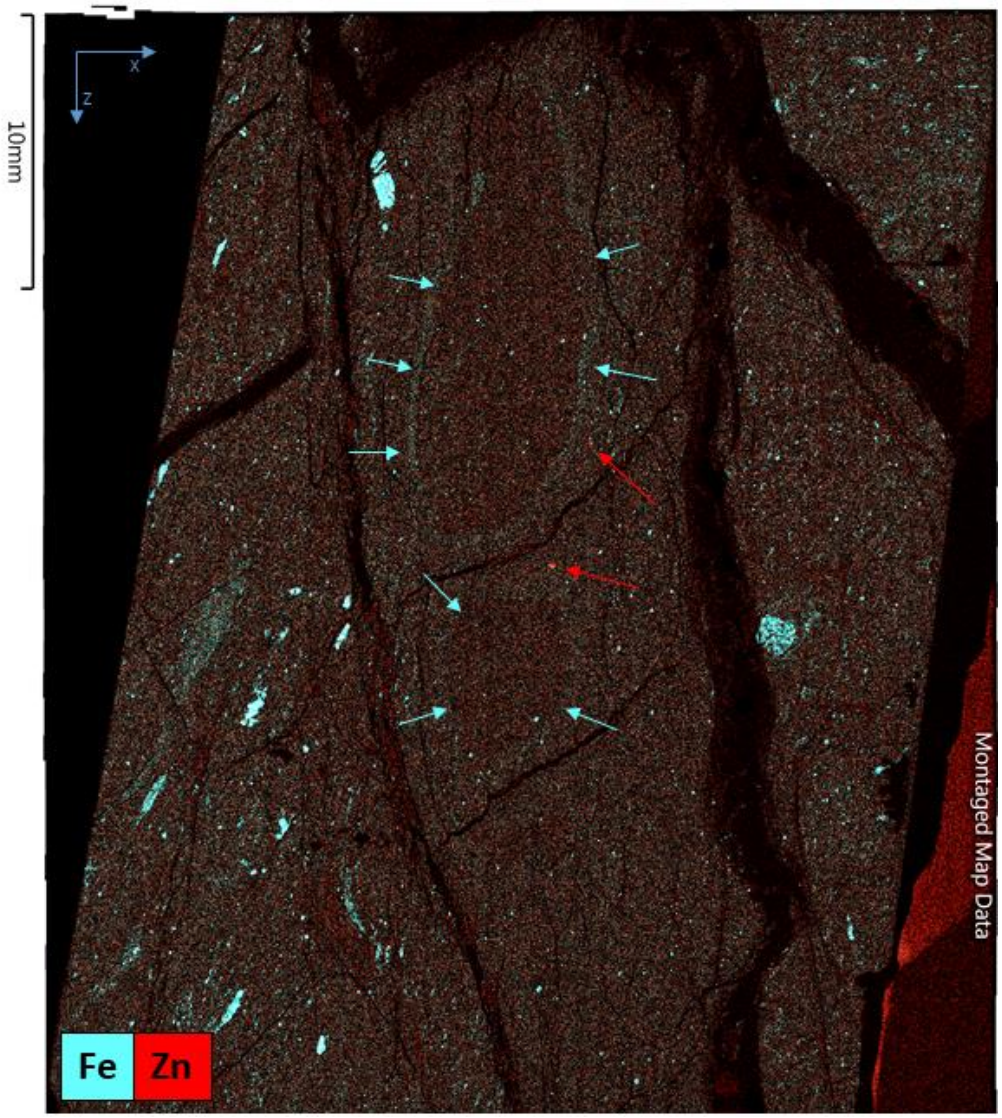

Figure 30. SEM-EDS map of iron and zinc in the S3_03 sample. Red arrows indicate the location of sphalerite grains. Turquoise arrows display an iron concentration band surrounding the central part of the gouge. Consequently, iron appears to be less concentrated inside the low-porosity central gouge. Pyrite appears to be mostly absent inside the gouge, excluding the large pyrite-domino in the upper left part of the gouge.

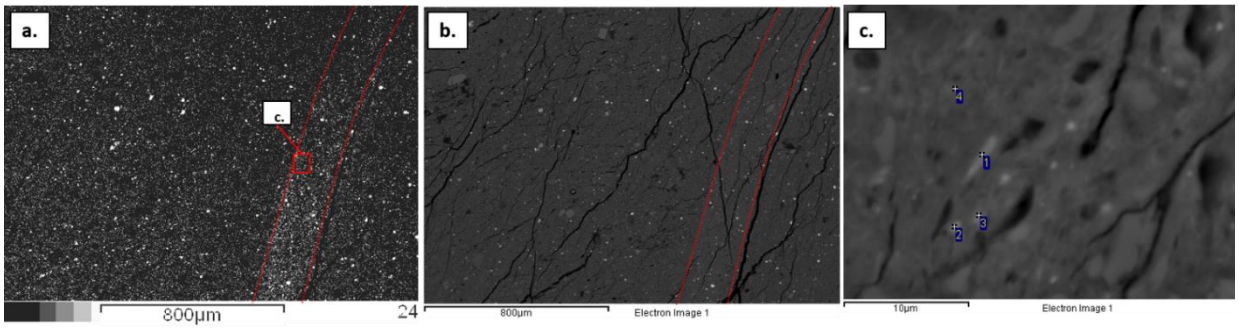

Figure 31. a.: an EDS elemental map of iron from the iron concentration zone of the gouge (indicated by red dashes). **b.**: a BSE image from the same zone. **c.**: a SEM image with EDS point analysis (1-4). All the EDS points indicate chamosite (Fe-end member of chlorite-group).

When the porosity maps from AGs are compared with elemental maps, iron appears to be located along fractures and surrounds the areas of lowest porosity within the gouge (Figure **32.**). Potassium appears to be depleted in the gouge interior but does not follow the fractures. The brecciated zone (BZ) is more depleted from potassium than the damaged zone. Calcium is absent inside the gouge 1. It exists abundantly in the DZ and BZ rock matrix and as micro-veins. The brecciated zone has therefore higher carbonate content and contains less clay minerals. This could indicate fault healing process in the breccia and strengthening of the eastern side of the gouge.

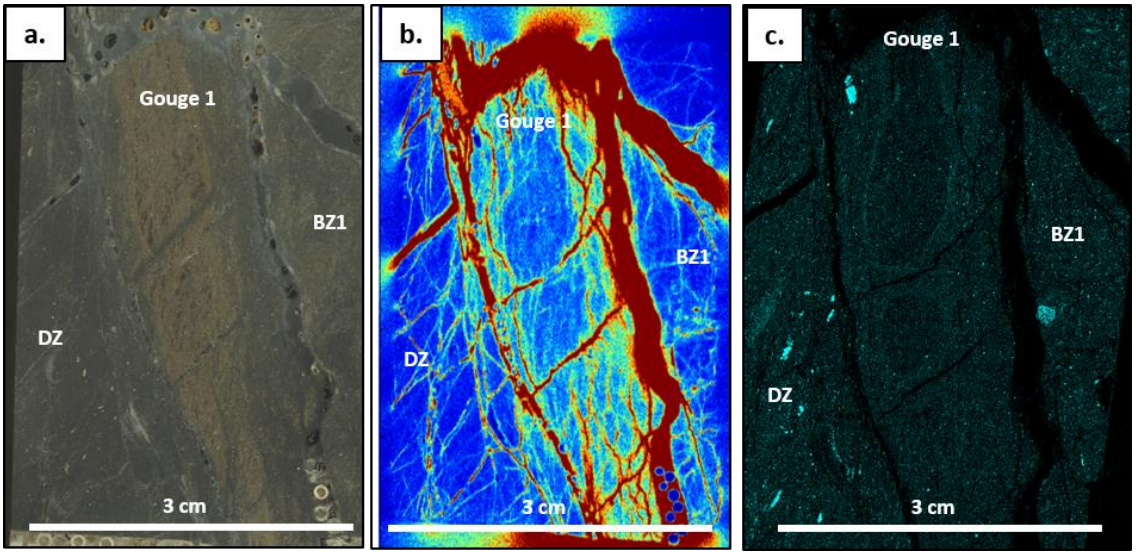

Figure 32. a.: scan of the sample S3_03 surface. **b.**: porosity color map of S3_03 surface. **c.**: SEM-EDS elemental map of iron.

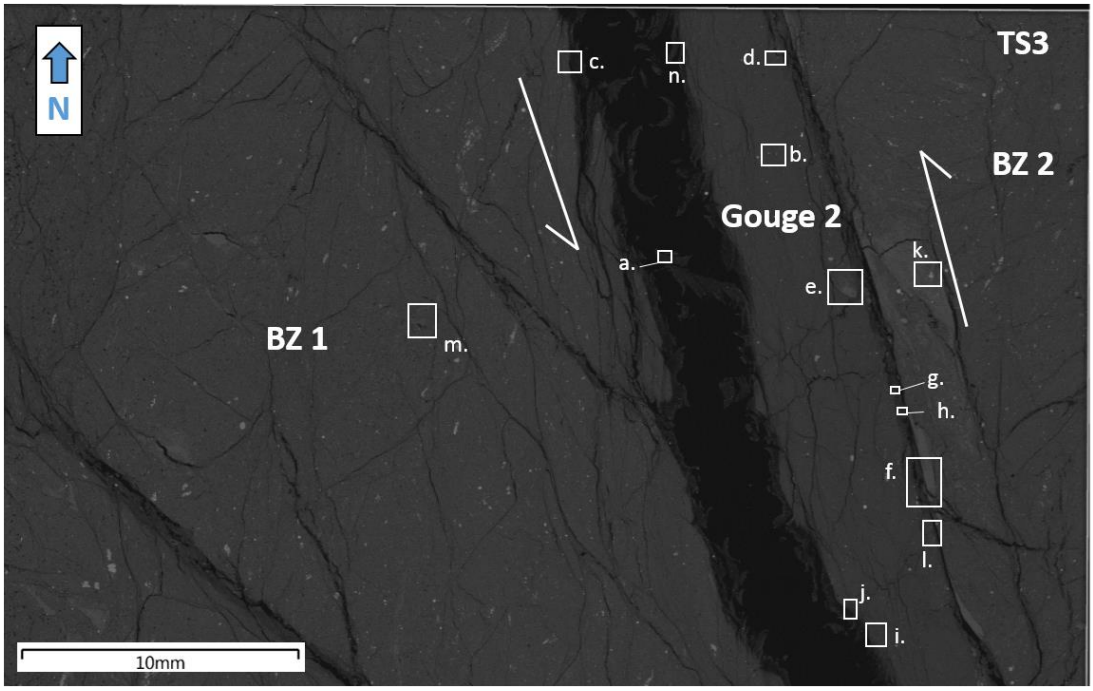

Figure 33. SEM-BSE image of the TS3 surface with Gouge 2. SEM images a.- m. in Figure **34**.

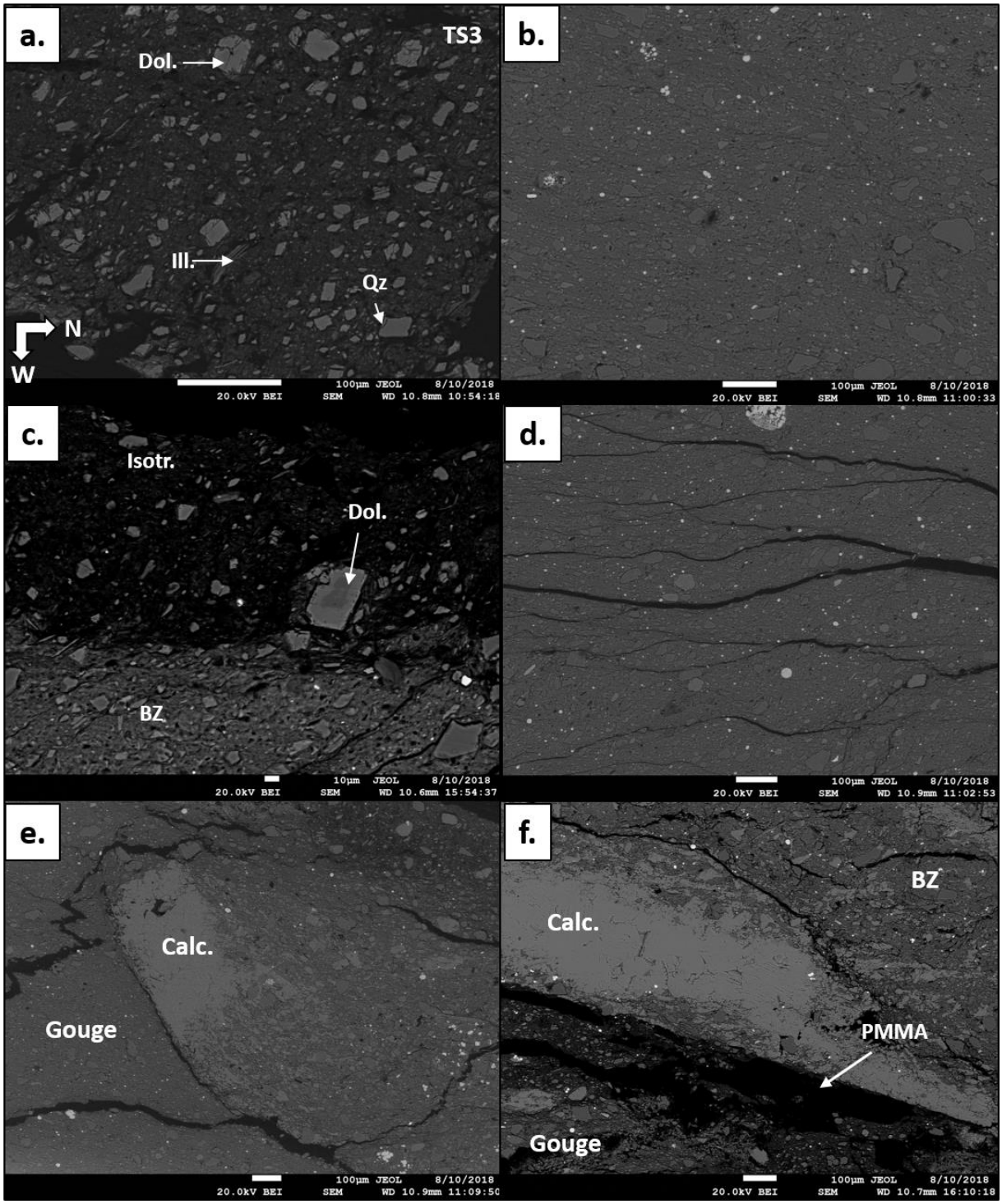
a.
TS3
Dol.
Ill.
Qz
N
W
100µm JEOL 8/10/2018
20.0kV BEI SEM WD 10.8mm 10:54:18
b.
100µm JEOL 8/10/2018
20.0kV BEI SEM WD 10.8mm 11:00:33
c.
Isotr.
Dol.
BZ
10µm JEOL 8/10/2018
20.0kV BEI SEM WD 10.6mm 15:54:37
d.
100µm JEOL 8/10/2018
20.0kV BEI SEM WD 10.9mm 11:02:53
e.
Calc.
Gouge
100µm JEOL 8/10/2018
20.0kV BEI SEM WD 10.9mm 11:09:50
f.
BZ
Calc.
PMMA
Gouge
100µm JEOL 8/10/2018
20.0kV BEI SEM WD 10.7mm 16:10:18

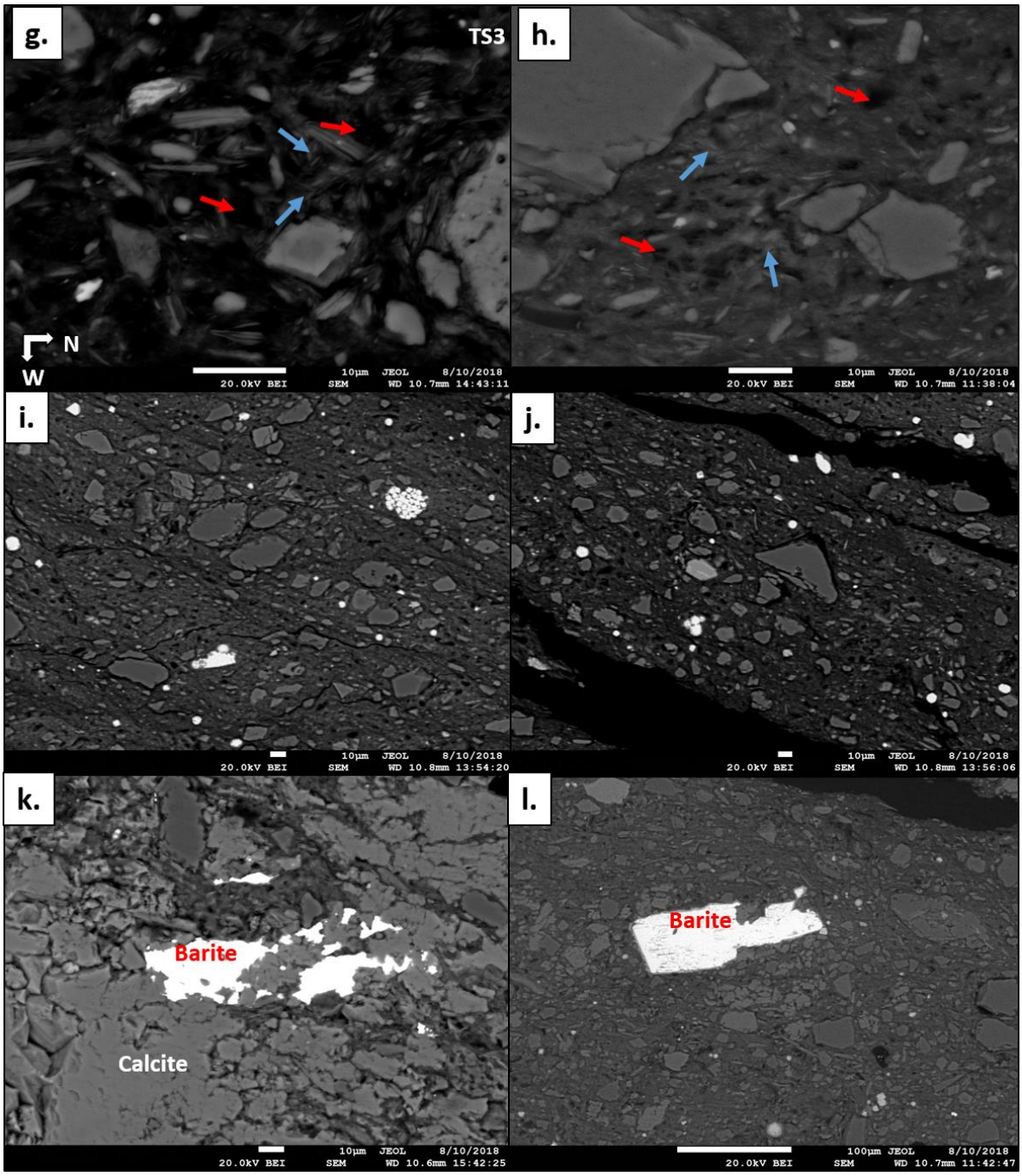
g.
TS3
N
W
20.0kV BEI 10µm JEOL SEM 8/10/2018 WD 10.7mm 14:43:11
h.
20.0kV BEI 10µm JEOL SEM 8/10/2018 WD 10.7mm 11:38:04
i.
20.0kV BEI 10µm JEOL SEM 8/10/2018 WD 10.8mm 13:54:20
j.
20.0kV BEI 10µm JEOL SEM 8/10/2018 WD 10.8mm 13:56:06
k.
Barite
Calcite
20.0kV BEI 10µm JEOL SEM 8/10/2018 WD 10.6mm 15:42:25
l.
Barite
20.0kV BEI 100µm JEOL SEM 8/10/2018 WD 10.7mm 11:42:47

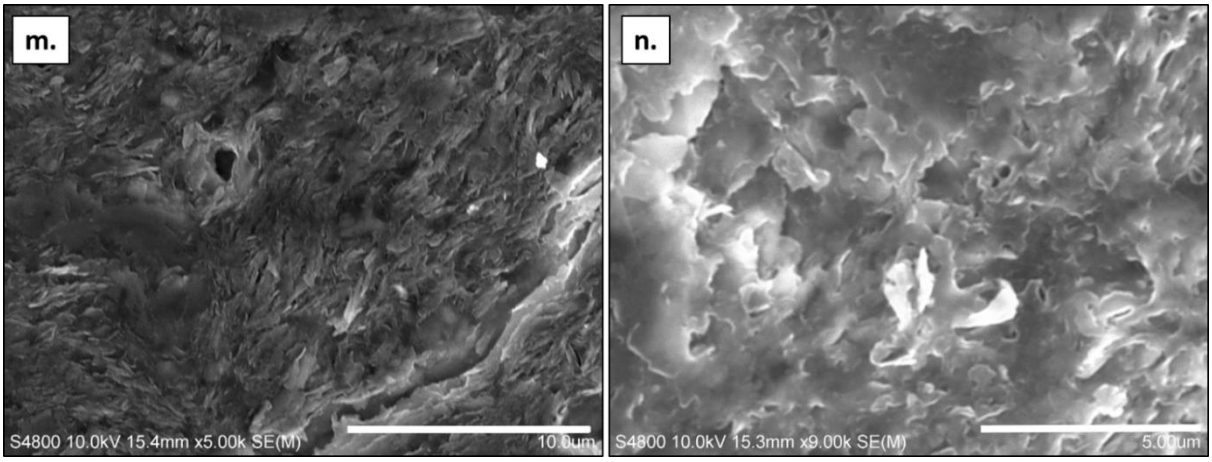

Figure 34. SEM images in BSE mode from the TS3 surface. All the images have the same orientation than in **a.** **a.**: Image from the highest porosity area of isotropic gouge between the BZ and Gouge 2. Dol.: dolomite, Ill.: illite. Clasts are mainly quartz, carbonates, illite and feldspars in very fine-grained clay matrix. Dolomite appears to be zoned with iron rich outer rim. Faint striations on the sample surface are from thin section polishing. **b.**: the lowest porosity area inside the Gouge 2. **c.**: BZ side of the highest porosity isotropic gouge. A sharp contact between the BZ1 and isotropic gouge. **d.**: Higher porosity area inside foliated gouge. **e.**: A calcite clast inside the foliated gouge. **f.**: a contact between the gouge and calcite crack-seal on the BZ3 side. Black areas are cracks filled by pure PMMA. **g.** and **h.**: the area with highest porosity between the gouge and BZ. Red arrows indicate empty pore spaces in clay matrix. Blue arrows indicate randomly oriented illite grains. **i.**: Shear bands and fractured quartz clasts inside gouge. **j.**: Quartz grains in the highest porosity zone in gouge-BZ interface. **k.** and **l.**: Anhedral and euhedral barite grains. **m.**: Detrital, foliated illite crystals in the breccia. Secondary electron (SE) image. **n.**: Neoformed, randomly oriented illite crystals in the isotropic gouge. SE image.

The area with highest AG porosity is indicated by a darker zone on the gouge-BZ boundary in the BSE image (Figure **33**.). Furthermore, the highest porosity gouge area appears to be isotropic and no clear foliations could be observed (Figure **34a.**). The boundary between the isotropic gouge and BZ is sharp (Figure **34c.**).

Grain rotations and cross-grain fractures indicate cataclastic flow inside the foliated gouge (Figure **34b.**). The major source of porosity appears as micro-fissures inside the higher porosity gouge area (Figure **34d.**). Calcite is abundant on the Gouge 2-BZ3 interface both inside the gouge and breccia. In gouge, calcite appears mainly as grains cementing spaces between clay minerals.

From TS3 SEM images, it was apparent that the Gouge 2 and BZ3 boundary contained barite (Figure **34k.** and **34l.**). Barite grains were both euhedral and anhedral and occurred within the calcite-rich zone but not anywhere else. SEM-EDS elemental map of calcite revealed that it is highly concentrated on the eastern side of the gouge zone. On the western side of the gouge, calcite does not form micro-veins (Figure **35a**, Figure **36.**). Pyrite grains are mostly absent inside Gouge 2 (Figure **35c.**).

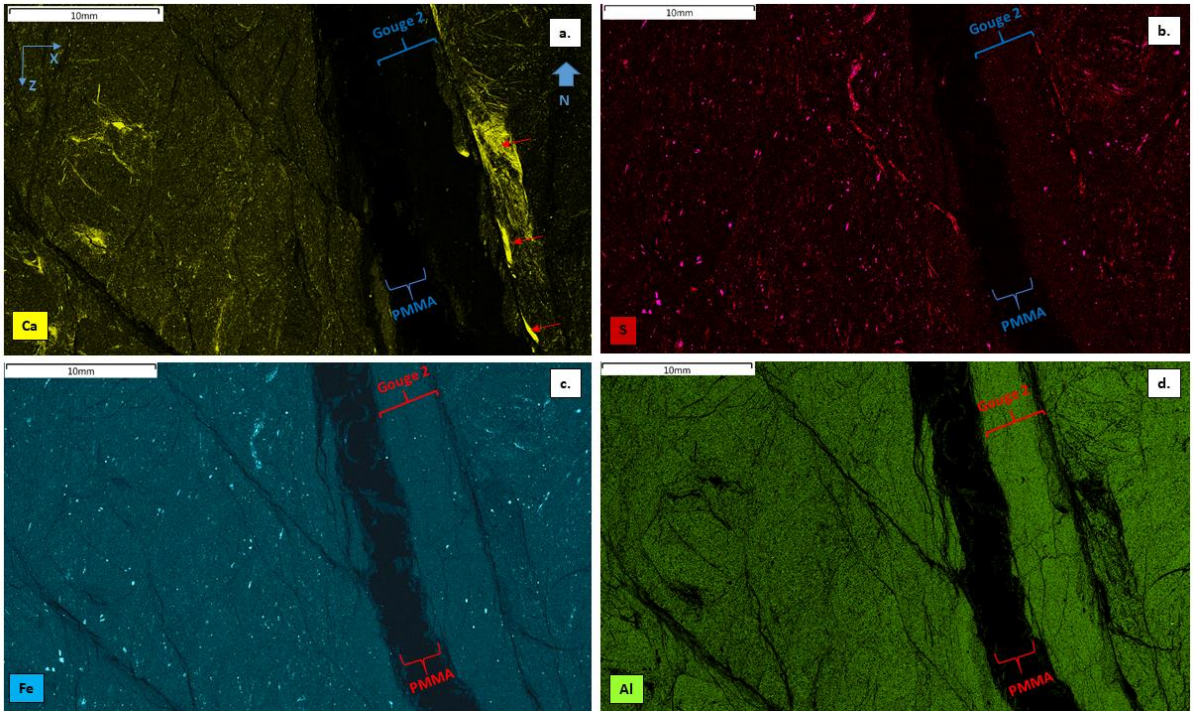

Figure 35. SEM-EDS elemental maps of TS3 thin section. **a.**: The locations of Gouge 2 and PMMA filled fracture are indicated. The image contains the concentrations of calcium. **b.**: The concentration of sulphur. **c.**: The content of iron. **d.**: The content of aluminium.

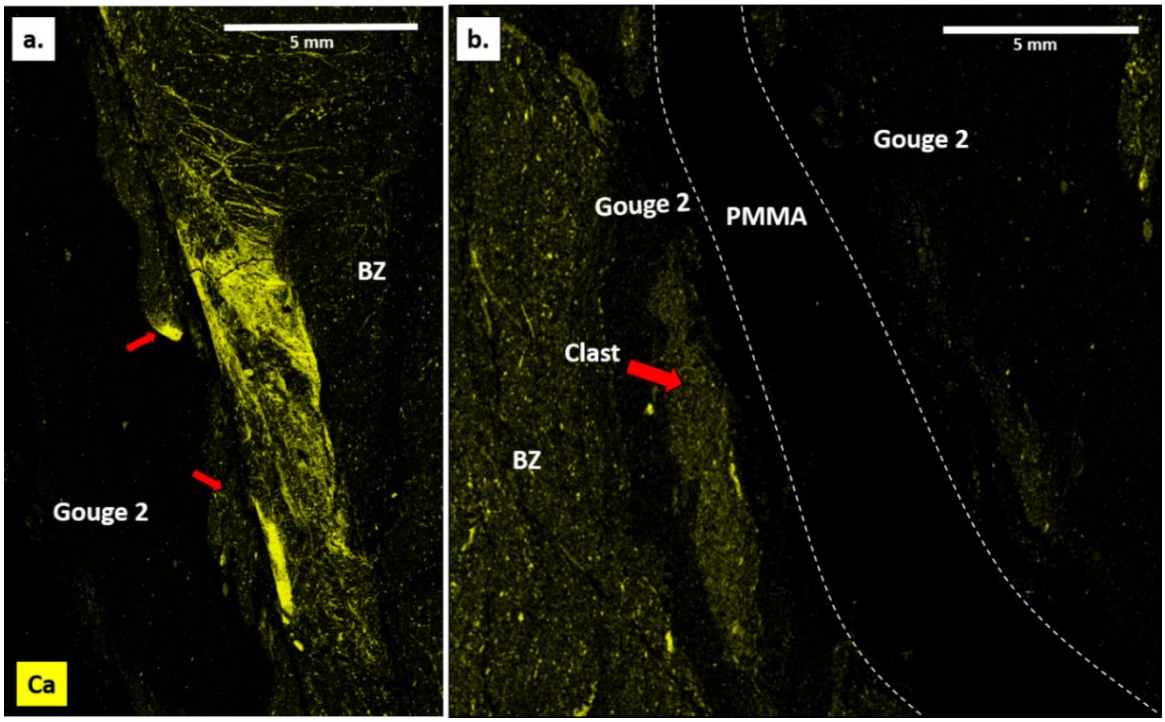

Figure 36. **a.**: A SEM-EDS elemental map of calcium from the Gouge 2 and BZ interface with calcite crack-sealing. Red arrows point ca-bearing gouge and a calcium clast inside the gouge. **b.**: A SEM-EDS map of calcium with a carbonatic clast inside the Gouge clast indicated by a red arrow. The black area in the centre is a fracture filled with pure PMMA.

The closer observation of Gouge 2 calcite-rich area indicates fluid-rock interactions with the gouge, brecciated area and fluids. The crack sealing could be a dilatational jog between the gouge and a gouge-parallel secondary fracture. Sphalerite was found on both gouges on areas with lowest amount of calcite grains. In Table **3**. is a summary of the EDS mapping and point analysis results for each domain.

Table 3. SEM-EDS mineralogy results tabulated for each structural domain.

	Undeformed shale	DZ	Interior gouge	Gouge/BZ 1 /2 side	Gouge/BZ 3 side	BZ 3
Gouge 1	K-rich clays (e.g. Lefèvre et al., 2016)	Clays, Py, Calcite	Clays, depleted in Ca	Clays, depleted in Ca, ZnS, Fe		
Gouge 2	K-rich clays		Clays, depleted in Ca	Clays, depleted in Ca, ZnS	Rich in Ca, Barite	Rich in Ca, Barite

In Figure **37**. is a tabletop scan from Gouge 2 in TS3 with a porosity colour map and a BSE image. Fractures exhibit the highest porosity values. Inside the BZ1, Gouge 2 oblique fractures crosscut the formation and are distinguishable by their higher porosity values. Inside BZ2 close to Gouge 2, crack-seals form very low porosity areas.

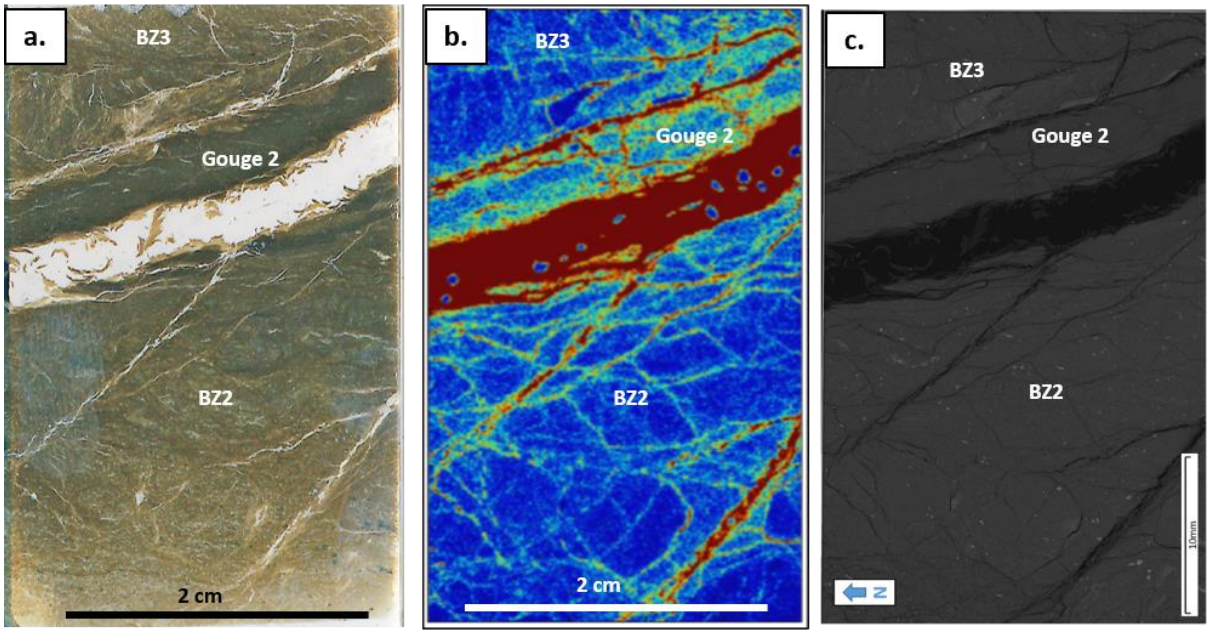

Figure 37. a.: Tabletop scan of TS3 thin section. **b.**: Porosity colour map of TS3. **c.**: BSE image of TS3.

Table 4. Porosity values and SEM-EDS mapping and XRD results for each structural domain in Tournemire shale and studied fault zone. Error (~10 %) is from autoradiography (Sammaljärvi et al., 2012).

Gouge 1	Undeformed shale	DZ	Interior gouge	Gouge/DZ side	Gouge/BZ 1 side	BZ 1
Porosity %	11 (Dick et al., 2016).	16 (± 2)	18 (± 2)	30 (± 3)	40 (± 4)	18 (± 2)
Predominant mineralogy	K-rich clays	Clays, Py	K-depleted clays, rich in S	Rich in K, Fe	Rich in K, Fe, ZnS	Rich in Ca
Kübler index		1.34	0.47		0.44	0.51

Gouge 2	Undeformed shale	BZ 2	Interior gouge	Gouge/BZ 2 side	Gouge/BZ 3 side	BZ 3
Porosity %	11 (Dick et al., 2016).	13 (± 1)	20 (± 2)	50 (± 5)	13 (± 1)	35 (± 4)
Predominant mineralogy	K-rich clays	Clays, Py, Calcite	clays, depleted in Ca	Clays, depleted in Ca, ZnS	Rich in Ca, Barite	Rich in Ca, Barite
Kübler index		1.27	0.78		0.63	0.63

Table **4.** presents a summary of results from different methods for each structural domain. The most significant feature separating Gouge 2 from Gouge 1 is that iron does not appear in spherical concentration bands (Figure **35c.**). Additionally, no signs of barite were observed in Gouge 1. Sphalerite grains were found inside the gouge areas without calcite grains. This highlights the complexity and different fluid sources of intrusions within the fault zone.

5. DISCUSSION

5.1. C-14-PMMA porosity

Because the fault zones evolve through time, they can act barriers to fluid flow during certain periods and conduits during other periods. Likewise, the porosity of the fault zone evolves through time due to numerous different chemical and physical processes.

Decreased effective normal stress leading to tensile fractures and dilatancy in the fault gouges could explain the observed porosity development. This can be seen as increasing porosity in the margins of the fault gouges, as shown by autoradiographs. Central gouge appears to have preserved mostly the barrier attributes. SEM images from the central part revealed that it is relatively fracture free and did not exhibit as high deformation rates as the gouge margins. The lower porosity of the central gouge could be due to extensive compaction and very fine-grained clay matrix. Moreover, the gouge matrix is matrix supported and clast rotation has apparently closed pore throats. However, towards the gouge margin strain rate increases and becomes more complex. Signs of extensive cataclastic flow and R- and P-foliation bands can be observed in the higher porosity areas. This could indicate strain localization to the highest porosity gouges, which possibly were the principal slip surfaces during the last sinistral shearing event. Shear foliations provide evidence that both gouges were active during the last sinistral phase of the Pyrenean orogeny. The damage zone and brecciated zones present partially very low porosities. The presumable reason for this lowering porosity is that the fault has healed on the damage zone side of the gouge and the cracks are filled with very low porosity calcite.

The C-14-PMMA autoradiography results highlighted the porosity anisotropy in the studied fault zone. When combined with optical microscopy, it was apparent that the highest porosity areas were concentrated on the gouge margins with fractures oriented to the shear stress of the fault. Strike-slip faults are generally more effective fault-parallel fluid conduits for crustal fluids than dip-slip faults due to fracture and stress orientation (Gudmundsson, 2001). Furthermore, strike-slip shearing experiments suggest that shearing-induced dilatancy may increase the permeability of a fault core (e.g. Samuelson et al., 2009). During the shearing pore space is created more on the margins of the gouge as the slip-velocity increases from centres to the margins of gouges. The pore-fluid then diffuse into the gouge layer and fill up the void created by shearing. This will lead to depressurization of the pore fluid, which inhibits the seismic nucleation of a fault and promotes fault creep behaviour instead of rupturing (Samuelson et al., 2009). Richard et al. (2014) found polymineralic clasts inside San Andreas (SAFOD) core of the creeping section. Similar almond-shaped clasts were found in Tournemire fault core (Figure **28f**.). Polymineralic clasts are proposed to be parts of original wall-rock reworked by dynamic fluid-induced shearing (Richard et al., 2014).

5.2. Connection of porosity, mineralogy and paleo-fluid circulation

Based on the AG-maps and SEM-EDS investigations it appears that the fluid flow occurred mainly along the high porosity gouge margin. Previous episodes which led to the calcification of the DZ confined the later fluid flow into the thin zone within the boundary between the gouge and DZ/BZ. Apparently, some of the fluid flow occurred inside the gouge zones. This is indicated by the iron concentration bands that follow the fracture boundaries within the gouge. The EDS investigations suggest that iron is mainly bound in chlorite-group minerals. Fe-rich chlorites are unstable in oxidizing conditions (Steudel et al., 2016) and may have formed from heat flow from hydrothermal fluids to the margins of lowest porosity gouge in Gouge 1. Even though fluid flow was mainly confined into vertical direction, some of the cross-gouge fractures in Gouge 1 could had provided a horizontal pathway for it. In these fractures, signs of shearing and calcite healing were absent. The fractures were possibly opened during the fault activation after a pore fluid pressure build-up exceeded the threshold needed for fault reactivation.

Elemental distribution of S received from the EDS elemental mapping indicates the concentration of sulphur to be higher on the western side of gouge in the DZ as pyrite. Additionally, S concentration appears to be higher in the low porosity central gouge in Gouge 1. Further, EDS maps from the elemental distribution indicate iron concentration bands, sphalerite in certain parts, and possibly hydrothermal circulation in the past. Barite in the Gouge 2 calcite-rich side has occurred most likely in co-precipitation with calcite from Ba-rich fluids. Possible source for Ba could be within basal fluids induced by Tertiary volcanism. Other possible source for fluids could had been brines from degassing of a cooling magmatic intrusion (Fournier, 1999). However, confirming the sources for fluids would require isotopic studies from mineral veins (e.g. Cox, 2007). Plummer (1971) concluded that barite deposits in hydrothermal fault systems could form by mixing of Ba-bearing reduced hydrothermal fluid and oxidizing meteoric fluid from an aquifer, with two fluid sources. In the Tournemire shale, the overlying aquifer could had been the source for oxidizing water influx (Peyaud et al., 2006).

SEM-EDS mapping showed the higher kaolinite content and sub-millimetric calcite veins within the gouge and adjacent DZ and BZ which provide evidence for the mineralogical evolution of the fault core. The XRD results indicating increasing kaolinite in the fault gouge is consistent with other studies from the same zone (Moreno et al., 2018; Dick et al., 2016).

The kaolinite increase in the gouge zones reflects a change in chemical and fluid–rock conditions and could indicate clay alteration due to a fluid circulation (Rossetti et al., 2010). In addition to cataclastic deformation, the clay-rich fault gouge could represent smear from an overlying clay-rich formation (Laurich et al., 2018). Such formation has not been identified in Tournemire however.

5.3. Clay-mineral alteration

The semi-quantitative results from XRD indicate transition of smectite-illite interstratifications into illite in the fault gouge. The amount of smectite-illite interstratifications diminish in respect to the damage zone. In the foliated gouge zone, the amount of I/S dropped and kaolinite and illite content appeared to increase. Moreover, in the anisotropic gouge, I/S disappears as seen in section Gouge 1b of Figure **26.** The transformation of smectite and illite-smectite into illite and chlorite within fault gouge generally requires temperatures exceeding 75 °C (Altaner and Ylagan, 1997; Inoue, 1995). This process could be caused by increased temperature due to shear friction, or alternatively hydrothermal fluid alteration (Ylagan et al., 2000). The main process to I/S alteration is possibly dissolution-crystallization (DC), which requires dissolving of original clay minerals and re-crystallizing them as neo-formed clay minerals (Dellisanti et al., 2008; Altaner and Ylagan, 1997). This could possibly explain the occurrence of increased potassium content observed in EDS-elemental mapping in section (Fig. **29 a.**) in the margin of Gouge 1 with neo-formation of illite. Additionally, smectite could had been altered into kaolinite, if hydrothermal temperature exceeded 150 °C during the fluid circulation phase (Dudek et al., 2007). Illite crystallinity (IC) values for gouges differ significantly from the damage zone (0.44 – 0.63 for gouges, 1.34 for the damage zone). Moreover, the breccias adjacent very closely to gouges have similar IC values. Observed IC values indicate that the gouges and breccias were influenced by temperatures 150 – 200 °C (Abad, 2007). The maximum diagenetic temperature in the Tournemire shale is estimated to be around 105 °C (Peyaud et al., 2005). The gouges and breccias therefore were affected either by frictional heating and/or hydrothermal fluids during their history.

The iron rim in the central Gouge 1 contains chlorite. One possible explanation for chlorite could be the alteration of smectite hydrothermally into chlorite (Inoue, 1995). When smectite dissolves, it releases the iron cations from the lattice structure. This iron could then

concentrate into neo-formed chlorite, forming the observed iron-rich rim. Frictional heating is short-termed and could not likely provide time needed for heat-induced alteration and neoformation of clay-minerals observed. Hydrothermal fluid circulation however, could provide a longer lasting heat source for the alteration process (Inoue, 1995).

5.4. Fault structure and dynamics

Clay gouge transformation and release of interlayer water of smectite due to shearing would require high slip-velocity, shear localization and high friction heat. The frictional heating increases the pore pressure in the shear zone. The result conceivably would be thermal pressurization within the fault gouge (Brantut et al., 2010). Thermal pressurization is the pressurization of the pore-fluids and reduction in the effective normal stress, produced by the expansion of vaporized fluid from the frictional heating of a fault (Sibson, 1973). Thermal pressurization is usually connected to the formation of clay-clast aggregates (CCAs) (Boullier et al., 2009; Boutareaud et al., 2010; Han and Hirose, 2012). However, Han and Hirose (2012) concluded that in experimental settings CCAs can be produced at slip rates that are slower than seismic slip rates. It has therefore been suggested that CCAs can form on wide range of slip rates by clast rotation and not only by thermal pressurization (Janssen et al., 2014; Han and Hirose, 2012). It is therefore safer to assume that the clay-mineral alteration was caused mainly by hydrothermal fluids and/or fluid accompanied dynamic frictional shearing. In the Tournemire shales, the fluid circulation is localized mainly on the thin zone between the fault core and damage zone (Guglielmi et al., 2015b), where CCAs could be expected to be found. Pervasive fluid intrusions and post-seismic creep accompanied reworking of fault core material could, however, remove the signs of seismic movements (Holsdworth, 2004), and therefore the possibility of thermal pressurization could not be entirely ruled out in the Tournemire fault.

Calcite crack sealing and fault history can indicate further hydrothermal circulation. First calcite generation formed from the pore fluids co-seismically during shearing. Second calcites formed from hydrothermal fluid circulation, eventually sealing the fault. Fibrous calcites appear stretched and grain growth localisation varies. This indicates multiple crack-sealing events and the localisation of grain-growth (e.g. Bons et al., 2012). The low permeabilities of the fault gouge and the host rock probably were responsible for forced fluid overpressure

conditions in the fault core, leading to fault-parallel fluid flow that was confined to a narrow, millimetric zone (Sibson, 2000).

High pore pressure inhibits healing and sealing processes, low pore pressure and high effective stress can lead to seismic nucleation (Ikari et al. 2009). During the high pore pressures, the fault core would stay impermeable. High pore pressure generally weakens the fault system and promotes instability and slip at low-shear stresses (Imber et al., 2008). During its active phase, the Tournemire fault may have moved episodically with initial seismic slip followed by post-seismic creep. Moreover, surface roughness and uneven surface structure may promote seismic slip at some parts of the fault, whereas other parts of the fault with smoother surface may move with creep even during the same tectonic event (Sibson, 1994). Aseismically creeping faults can typically generate large numbers of small earthquakes and micro-seismic lineations, such as calcite crack-seals and other microscale features observed (Rubin et al., 1999).

5.5. Future work

The dating of tectonic events and associated fluid circulations would require further work and isotopic dating methods. K-Ar dating of clay minerals requires neoformed illite crystals. Such neoformations has indications inside the Tournemire F2 gouge zones suggested by the results. Isotopic fractionations of oxygen and sulphur from carbonate and sulphate minerals of the fault zones could reveal more from the origin and formation temperatures of these mineralizations. X-ray computed tomography (XRCT) could be utilized to obtain a mesoscale 3D-image of the fault gouge structure (Sammaljärvi et al., 2017). Preliminary results for XRCT imaging from the Tournemire fault gouge were presented by Nenonen et al. (2018). Higher resolution images would require more XRCT artefact removal however.

6. CONCLUSIONS

In this work, the spatial porosity distribution in the Tournemire URL strike-slip fault was investigated. Samples from the fault core were impregnated with ^{14}C-PMMA to obtain a

porosity map from the gouge zones. Smaller samples from PMMA-impregnated block were investigated with photomicroscope, SEM-EDS and XRD.

The structure of the fault could indicate a polyphased structural history, where the subhorizontal cleavage presents the initial fault zone. Fault reactivation in this zone is interpreted to has been led to the formation of a new fault zone containing the fault core with several distinct gouges. Porosity maps obtained from AG indicate porosity anisotropy within the studied gouge zone. The fault gouge is zoned, with lower porosity towards the center and higher near the borders. SEM-EDS elemental maps revealed the uneven distribution of Fe, K and Ca containing minerals. The mineral zonation indicates complex fluid circulation, with both high and low temperature hydrothermal activities. Possible explanation for the porosity increasing in the sub-millimeter zone between the gouges and the wall/breccia could be thermal pressurization of water released from the illite-smectite interlayers via high-velocity shearing friction. The expanding water vapor lead to drop in the effective normal stress within the gouge and dilation, which is indicated by increased porosities. The fluid vapor most likely escaped vertically, as the gouge center remained with low porosity. This dilation-channel eventually provided pathways for hydrothermal fluid-circulation induced by volcanism in the Central Massif area during the Paleo- and Neogene. The remains of this fluid-circulation were marked by an iron halo around the lowest porosity central gouge in the Gouge 1. Moreover, sphalerite crystals were found in the Gouge zone, which could be further explained by the hydrothermal fluid circulation.

Fault gouge exhibits signs of seismic slip and possibly post-seismic creep. During its active phase, the fault was healed by calcite precipitation after a seismic slip. This healing and sealing led to increasing pore pressure inside the fault core. The high pore pressure decreased the strength of the fault and promoted fault slip. Fault was reactivated during the sinistral phase seismically or aseismically. During the last sinistral shearing, fault movement occurred mostly by fluid induced brittle-viscous creep behavior. However, the fault may have partially moved seismically due to roughness of the fault core surface.

Although these fault gouges in shale formations are only several millimeters thick, they may provide preferential pathways for fluid circulation during fault reactivation. They can offer a barrier or a conduit to localized fluid flow within the fault zone. Based on the results, there is a possibility that in case of Gouge 1 and Gouge 2, gouge allowed fault-parallel fluid flow through the gouge zone and thus compromised the barrier. The understanding of these gouges

is thus essential when performing performance assessments of potential fractured clay host rocks for geological storage.

7. REFERENCES

Abad, I. (2007). Physical meaning and applications of the illite Kübler index: measuring reaction progress in low-grade metamorphism. *Diagenesis and Low-Temperature Metamorphism. Theory, Methods and Regional Aspects. Seminarios de la Sociedad Española de Mineralogía, Jaén*, 53 – 64.

Altaner, S. P., and Ylagan, R. F. (1997). Comparison of structural models of mixed-layer illite/smectite and reaction mechanisms of smectite illitization. *Clays and Clay Minerals, 45*, 517 – 533.

Barbarand, J., Lucazeau, F., Pagel, M., and Séranne, M. (2001). Burial and exhumation history of the south-eastern Massif Central (France) constrained by apatite fission-track thermochronology. *Tectonophysics, 335*, 275 – 290.

Biscaye, P. E. (1965). Mineralogy and sedimentation of recent deep-sea clay in the Atlantic Ocean and adjacent seas and oceans. *Geological Society of America Bulletin, 76*, 803 – 832.

Blanpied, M. L., Lockner, D. A., and Byerlee, J. D. (1992). An earthquake mechanism based on rapid sealing of faults. *Nature, 358*, 574 – 576.

Bons, P. D., Elburg, M. A., and Gomez-Rivas, E. (2012). A review of the formation of tectonic veins and their microstructures. *Journal of Structural Geology, 43*, 33 – 62.

Boullier, A. M., Yeh, E. C., Boutareaud, S., Song, S. R., and Tsai, C. H. (2009). Microscale anatomy of the 1999 Chi-Chi earthquake fault zone. *Geochemistry, Geophysics, Geosystems, 10*, Q03016.

Boutareaud, S., Boullier, A.-M., Andréani, M., Calugaru, D.-G., Beck, P., Song, S.-R., and Shimamoto, T. (2010). Clay clast aggregates in gouges: New textural evidence for seismic faulting. *Journal of Geophysical Research, 115*, B02408.

Brantut, N., Schubnel, A., Corvisier, J., and Sarout, J. (2010). Thermochemical pressurization of faults during coseismic slip. *Journal of Geophysical Research: Solid Earth, 115*, B05314.

Byerlee, J. (1993). Model for episodic flow of high-pressure water in fault zones before earthquakes. *Geology, 21*, 303 – 306.

Caine, J. S., Evans, J. P., and Forster, C. B. (1996). Fault zone architechture and permeability structure. *Geology, 24*, 1025 – 1028.

Chester, F. M., Evans, J. P., and Biegel, R. L. (1993). Internal structure and weakening mechanisms of the San Andreas Fault. *Journal of Geophysical Research: Solid Earth, 98*, 771 – 786.

Constantin, J., Laurent, P., Vergély, P., and Cabrera, J. (2007). Paleo-deviatoric stress magnitudes from calcite twins and related structural permeability evolution in minor faults: Example from the toarcian shale of the French Causses Basin, Aveyron, France. *Tectonophysics, 429*, 79 – 97.

Constantin, J., Peyaud, J. B., Vergély, P., Pagel, M., and Cabrera, J. (2004). Evolution of the structural fault permeability in argillaceous rocks in a polyphased tectonic context. *Physics and Chemistry of the Earth, 29*, 25 – 41.

Cox, S. F. (2007). Structural and isotopic constraints on fluid flow regimes and fluid pathways during upper crustal deformation: an example from the Taemas area of the Lachlan Orogen, SE Australia. *Journal of Geophysical Research: Solid Earth, 112*, B08208.

Delage, P., Cui, Y. J., and Tang, A. M. (2010). Clays in radioactive waste disposal. *Journal of Rock Mechanics and Geotechnical Engineering, 2*, 111 – 123.

Dellisanti, F., Pini, G. A., Tateo, F., and Baudin, F. (2008). The role of tectonic shear strain on the illitization mechanism of mixed-layers illite–smectite. A case study from a fault zone in the Northern Apennines, Italy. *International Journal of Earth Sciences, 97*, 601 – 616.

Dick, P., Wittebroodt, C., Courbet, C., Sammaljärvi, J., Siitari-Kauppi, M., Esteve, I., Matray, J.M.,

and Dauzeres, A. (2016). The Internal Architecture and Permeability Structures of Faults in Shale Formations, In *The Clay Minerals Society Workshop Lectures Series*, *21*, 227 – 242.
Dockrill, B., and Shipton, Z. K. (2010). Structural controls on leakage from a natural CO_2 geologic storage site: Central Utah, U.S.A. *Journal of Structural Geology*, *32*, 1768 – 1782.
Dudek, T., Cuadros, J., and Huertas, J. (2007). Structure of mixed-layer kaolinite-smectite and smectite-to-kaolinite transformation mechanism from synthesis experiments. *American Mineralogist*, *92*, 179 –192.
Engelder, J. T. (1974). Cataclasis and the Generation of Fault Gouge. *Bulletin of the Geological Society of America*, *85*, 1515 – 1522.
Friel, J. J. (2003). *X-ray and image analysis in electron microscopy*. Princeton Gamma-Tech Incorporated, Princeton, New Jersey, 88 p.
Moreno, E., Homberg, C., Schnyder, J., Person, A., David, C., du Peloux, A., and Dick, P. (2018). Fault imprint in clay units: Magnetic fabric, p-wave velocity, structural and mineralogical signatures. *Tectonophysics*, *745*, 264 – 277.
Ewing, R. C. (2015). Long-term storage of spent nuclear fuel. *Nature Materials*, *14*, 252 – 257.
Faulkner, D. R., Jackson, C. A. L., Lunn, R. J., Schlische, R. W., Shipton, Z. K., Wibberley, C. A. J., and Withjack, M. O. (2010). A review of recent developments concerning the structure, mechanics and fluid flow properties of fault zones. *Journal of Structural Geology*, *32*, 1557 – 1575.
Fournier, R. O. (1999). Hydrothermal processes related to movement of fluid from plastic into brittle rock in the magmatic-epithermal environment. *Economic Geology*, *94*, 1193 – 1211.
Gudmundsson, A. (2001). Fluid overpressure and flow in fault zones: Field measurements and models. *Tectonophysics*, *336*, 183 – 197.
Guglielmi, Y. G., Henry, P., Nussbaum, C., Dick, P., Gout, C., and Amann, F. (2015a). Underground Research Laboratories for conducting fault activation experiments in shales. In *49th US Rock Mechanics/Geomechanics Symposium*, *2*, 1072 – 1077, American Rock Mechanics Association.
Guglielmi, Y. G., Elsworth, D., Cappa, F., Henry, P., Gout, C., Dick, P., and Durand, J. (2015b). In situ observations on the coupling between hydraulic diffusivity and displacements during fault reactivation in shales. *Journal of Geophysical Research: Solid Earth*, *120*, 7729 – 7748.
Han, R., and Hirose, T. (2012). Clay-clast aggregates in fault gouge: An unequivocal indicator of seismic faulting at shallow depths? *Journal of Structural* Geology, *43*, 92 – 99.
Hellmuth, K.-H., Lukkarinen, S., and Siitari-kauppi, M. (1994). Rock Matrix Studies with Carbon-14-Polymethylmethacrylate (PMMA); Method Development and Applications. *Isotopenpraxis Isotopes in Environmental and Health Studies*, *30*, 47 – 60.
Hellmuth, K. H., Siitari-Kauppi, M., and Lindberg, A. (1993). Study of porosity and migration pathways in crystalline rock by impregnation with 14C-polymethylmethacrylate. *Journal of Contaminant Hydrology*, *13*, 403 – 418.
Hickman, S., Sibson, R., and Bruhn, R. (1995). Introduction to special section: Mechanical involvement of fluids in faulting. *Journal of Geophysical Research: Solid Earth*, *100*, 12831 – 12840.
Holdsworth, R. E. (2004). Weak faults - rotten cores. *Science*, *303*, 181 – 182.
Holland, M., Urai, J. L., van der Zee, W., Stanjek, H., and Konstanty, J. (2006). Fault gouge evolution in highly overconsolidated claystones. *Journal of Structural Geology*. *28*, 323 – 332.
Horseman, S. T., Winter, M. G., and Enwistle, D. C. (1987). *Geotechnical characterization of Boom clay in relation to the disposal of radioactive waste* (No. EUR-10987), Commission of the European Communities.
Ikari, M. J., Saffer, D. M., and Marone, C. (2009). Frictional and hydrologic properties of clay-rich fault gouge. *Journal of Geophysical Research: Solid Earth*, *114*, B05409.
Imber, J., Holdsworth, R. E., Smith, S. A. F., Jefferies, S. P., and Collettini, C. (2008). Frictional-viscous flow, seismicity and the geology of weak faults: a review and future directions. *Geological Society, London, Special Publications*, *299*, 151 – 173.
Inoue, A. (1995). Formation of clay minerals in hydrothermal environments. In *Origin and mineralogy of clays*, pp. 268 – 329, Springer, Berlin.
Jaboyedoff, M., Bussy, F., Kübler, B., and Thelin, P. (2001). Illite "crystallinity" revisited. *Clays and clay minerals*, *49*, 156 – 167.

Janssen, C., Wirth, R., Wenk, H. R., Morales, L., Naumann, R., Kienast, M., and Dresen, G. (2014). Faulting processes in active faults - Evidences from TCDP and SAFOD drill core samples. *Journal of Structural Geology*, *65*, 100 – 116.

Knipe, R. J. (1989). Deformation mechanisms - recognition from natural tectonites. *Journal of Structural Geology*, *11*, 127 – 146.

Kübler, B. (1964). Les argiles, indicateurs de métamorphisme. *Rev. Inst. Franc. Petrole.*, *19*, 1093 – 1112.

L'Annunziata, M. F. (2012). *Handbook of radioactivity analysis*, Academic Press, Amsterdam, Netherlands, 1365 p.

Laurich, B., Urai, J. L., Desbois, G., Vollmer, C., and Nussbaum, C. (2014). Microstructural evolution of an incipient fault zone in Opalinus Clay: Insights from an optical and electron microscopic study of ion-beam polished samples from the Main Fault in the Mt-Terri Underground Research Laboratory. *Journal of Structural Geology*, *67*, 107 – 128.

Laurich, B., Urai, J. L., Vollmer, C., and Nussbaum, C. (2018). Deformation mechanisms and evolution of the microstructure of gouge in the Main Fault in Opalinus Clay in the Mont Terri rock laboratory (CH). *Solid Earth*, *9*, 1 – 24.

Lavielle, B., Matray, J. M., Thomas, B., Dauzères, A., Bensenouci, F., and Gilabert, E. (2012). Stages of evolution of a Toarcian compacted claystone around galleries excavated between 1 and 124 years ago by the study of noble gases dissolved in pore water at the Tournemire Underground Research Laboratory (France). *Applied Geochemistry*, *27*, 1403 – 1416.

Lefèvre, M., Guglielmi, Y., Henry, P., Dick, P., and Gout, C. (2016). Calcite veins as an indicator of fracture dilatancy and connectivity during strike-slip faulting in Toarcian shale (Tournemire tunnel, Southern France). *Journal of Structural Geology*, *83*, 73 – 84.

Lloyd, G. E. (1987). Atomic number and crystallographic contrast images with the SEM: a review of backscattered electron techniques. *Mineralogical Magazine*, *51*, 3 – 19.

Matray, J. M., Savoye, S., and Cabrera, J. (2007). Desaturation and structure relationships around drifts excavated in the well-compacted Tournemire's argillite (Aveyron, France). *Engineering Geology*, *90*, 1 – 16.

Michon, L., and Merle, O. (2001). The evolution of the Massif Central rift: spatio-temporal distribution of the volcanism. *Bulletin de la Société Géologique de France*, *172*, 201 – 211.

Moore, D. M., and Reynolds, R. C. (1997). X-Ray diffraction and the identification and analysis of clay minerals,. *Oxford University Press*, Oxford, New York, 373 p.

Morrow, C. A., Shi, L. Q., and Byerlee, J. D. (1984). Permeability of fault gouge under confining pressure and shear stress. *Journal of Geophysical Research: Solid Earth*, *89*, 3193 – 3200.

Nenonen, V., Sammaljärvi, J., Johanson, B., Voutilainen, M., Dick, P., and Siitari-Kauppi, M. (2018). Porosity distribution in a heterogeneous clay-rich fault core by image processing of 14 C-PMMA autoradiographs and Scanning Electron Microscopy. *MRS Advances*, *3*, 1167 – 1173.

Peyaud, J. B., Pagel, M., Cabrera, J., and Pitsch, H. (2006). Mineralogical, chemical and isotopic perturbations induced in shale by fluid circulation in a fault at the Tournemire experimental site (Aveyron, France). *Journal of Geochemical Exploration*, *90*, 9 – 23.

Peyaud, J. B., Barbarand, J., Carter, A., and Pagel, M. (2005). Mid-Cretaceous uplift and erosion on the northern margin of the Ligurian Tethys deduced from thermal history reconstruction. *International Journal of Earth Sciences*, *94*, 462 – 474.

Pichler, H., and Schmitt-Riegraf, C. (1997). *Rock-forming minerals in thin section. Chapman & Hall*, Stuttgart, Germany, 220 p.

Plummer, L. N. (1971). Barite deposition in central Kentucky. *Economic Geology*, *66*, 252 – 258.

Poppe, L. J., Paskevich, V. F., Hathaway, J. C., and Blackwood, D. S. (2001). A Laboratory Manual for X-Ray Powder Diffraction. *U. S. Geological Survey Open-File Report 01-041*, 88 p.

Prêt, D., Sardini, P., Beaufort, D., Zellagui, R., and Sammartino, S. (2004). Porosity distribution in a clay gouge by image processing of 14C-PolyMethylMethAcrylate (14C-PMMA) autoradiographs: Case study of the fault of St. Julien (Basin of Lodève, France). *Applied Clay Science*, *27*, 107 – 118.

Robinet, J. C., Sardini, P., Coelho, D., Parneix, J. C., Prt, D., Sammartino, S., and Altmann, S. (2012). Effects of mineral distribution at mesoscopic scale on solute diffusion in a clay-rich rock: Example of the Callovo-Oxfordian mudstone (Bure, France). *Water Resources Research*, *48*, 1 –

17.
Robinet, J. C., Sardini, P., Siitari-Kauppi, M., Prêt, D., and Yven, B. (2015). Upscaling the porosity of the Callovo-Oxfordian mudstone from the pore scale to the formation scale; insights from the ^{3}H-PMMA autoradiography technique and SEM BSE imaging. *Sedimentary Geology, 321*, 1 – 10.
Rossetti, F., Aldega, L., Tecce, F., Balsamo, F., Billi, A., and Brilli, M. (2010). Fluid flow within the damage zone of the Boccheggiano extensional fault (Larderello–Travale geothermal field, central Italy): structures, alteration and implications for hydrothermal mineralization in extensional settings. *Geological Magazine, 148*, 558 – 579.
Richard, J., Gratier, J. P., Doan, M. L., Boullier, A. M., & Renard, F. (2014). Rock and mineral transformations in a fault zone leading to permanent creep: Interactions between brittle and viscous mechanisms in the San Andreas Fault. *Journal of Geophysical Research: Solid Earth*, *119*, 8132 – 8153.
Rubin, A. M., Gillard, D., and Got, J. L. (1999). Streaks of microearthquakes along creeping faults. *Nature*, *400*, 635.
Saffer, D. M., and Marone, C. (2003). Comparison of smectite-and illite-rich gouge frictional properties: application to the updip limit of the seismogenic zone along subduction megathrusts. *Earth and Planetary Science Letters*, *215*, 219 – 235.
Sammaljärvi, J. (2017). Structural characterisation via C-14-PMMA impregnation technique: Method and application development., Academic dissertation, *Report series in Radiochemistry, University of Helsinki*, *37*, 101 p.
Sammaljärvi, J., Lindberg, A., Voutilainen, M., Ikonen, J., Siitari-Kauppi, M., Pitkänen, P., and Koskinen, L. (2017). Multi-scale study of the mineral porosity of veined gneiss and pegmatitic granite from Olkiluoto, Western Finland. *Journal of Radioanalytical and Nuclear Chemistry*, *314*, 1557 – 1575.
Sammaljärvi, J., Shroff Rama, M., Ikonen, J., Muuri, E., Hellmuth, K.-H., and Siitari-Kauppi, M. (2016). Free radical polymerisation of methacrylates with thermal initiator in clay rock. *Engineering Geology*, *210*, 70 – 83.
Sammaljärvi, J., Jokelainen, L., Ikonen, J., and Siitari-Kauppi, M. (2012). Free radical polymerisation of MMA with thermal initiator in brick and Grimsel granodiorite. *Engineering Geology*, *135 – 136*, 52 – 59.
Sammartino, S., Bouchet, A., Prêt, D., Parneix, J. C., and Tevissen, E. (2003). Spatial distribution of porosity and minerals in clay rocks from the Callovo-Oxfordian formation (Meuse/Haute-Marne, Eastern France) - Implications on ionic species diffusion and rock sorption capability. *Applied Clay Science*, *23*, 157 – 166.
Sammartino, S., Siitari-Kauppi, M., Meunier, A., Sardini, P., Bouchet, A., and Tevissen, E. (2002). An Imaging Method for the Porosity of Sedimentary Rocks: Adjustment of the PMMA Method--Example of a Characterization of a Calcareous Shale. *Journal of Sedimentary Research*, *72*, 937 – 943.
Samuelson, J., Elsworth, D., and Marone, C. (2009). Shear-induced dilatancy of fluid-saturated faults: Experiment and theory. *Journal of Geophysical Research: Solid Earth*, *114*, 1 – 15.
Sardini, P., Caner, L., Mossler, P., Mazurier, A., Hellmuth, K. H., Graham, R. C., and Siitari-Kauppi, M. (2015). Calibration of digital autoradiograph technique for quantifying rock porosity using ^{14}C-PMMA method. *Journal of Radioanalytical and Nuclear Chemistry*, *303*, 11 – 23.
Sardini, P., El Albani, A., Prêt, D., Gaboreau, S., Siitari-Kauppi, M., and Beaufort, D. (2009). Mapping and Quantifying the Clay Aggregate Microporosity in Medium- to Coarse-Grained Sandstones Using the 14C-PMMA Method. *Journal of Sedimentary Research*, *79*, 584 – 592.
Sibson, R. H. (2000). Fluid involvement in normal faulting. *Journal of Geodynamics, 29*, 469 – 499.
Sibson, R. H. (1973). Interactions between Temperature and Pore-Fluid Pressure during Earthquake Faulting and a Mechanism for Partial or Total Stress Relief. *Nature*, *243*, 66 – 68.
Sibson, R. H. (1994). Crustal stress, faulting and fluid flow. *Geological Society, London, Special Publications*, *78*, 69 – 84.
Sibuet, J. C., Srivastava, S. P., and Spakman, W. (2004). Pyrenean orogeny and plate kinematics. *Journal of Geophysical Research: Solid Earth*, *109*, 1 – 18.
Steudel, A., Kleeberg, R., Koch, C.B., Friedrich, F., and Emmerich, K. (2016). Thermal behavior of chlorites of the clinochlore-chamosite solid solution series: Oxidation of structural iron,

hydrogen release and dehydroxylation. *Applied Clay Science. 132 – 133*, 626 – 634.
Siitari-Kauppi, M. (2002). Development of 14-C-polymethylmethacrylate method for the characterisation of low porosity media. Academic dissertation, *Report series in Radiochemistry, University of Helsinki, 17*, 156 p.
Van Der Pluijm, B. (2011). Structural geology: Natural fault lubricants. *Nature Geoscience, 4*, 217 – 218.
Vrolijk, P., and Van Der Pluijm, B. A. (1999). Clay gouge. *Journal of Structural Geology, 21*, 1039 – 1048.
Wibberley, C. A. J., Yielding, G., and Di Toro, G. (2008). Recent advances in the understanding of fault zone internal structure: a review. *Geological Society, London, Special Publications, 299*, 5 – 33.
Ylagan, R. F., Altaner, S. P., and Pozzuoli, A. (2000). Reaction mechanisms of smectite illitization associated with hydrothermal alteration from Ponza Island, Italy. *Clays and Clay Minerals, 48*, 610 – 631.